THE ASTROPHYSICAL JOURNAL, 448:395–415, 1995 July 20

HUBBLE SPACE TELESCOPE AND *R*-BAND ECLIPSE MAPS OF THE UX URSAE MAJORIS ACCRETION DISK[1]

R. BAPTISTA,[2] KEITH HORNE,[2,3,4] R. W. HILDITCH,[4] K. O. MASON,[5] AND J. E. DREW[6]

Received 1994 November 15; accepted 1995 January 30

ABSTRACT

Hubble Space Telescope time-resolved spectroscopic and ground-based *R*-band photometric data of UX UMa during eclipse are presented and discussed. The spectroscopy covers the C IV λ1550 and He II λ1640 spectral regions. The eclipses in the UV continuum are deep, nearly reaching the zero level at mid-eclipse phases. Sharp ingress and egress features reveal the occultation of the white dwarf at disk center but there is no evidence of the orbital hump or of the bright spot. The steep ultraviolet eclipse light curves are used to estimate the radius of the white dwarf and to constrain the binary parameters. We find $M_1 = M_2 = 0.47\ M_\odot$ and $i = 71\overset{\circ}{.}0 \pm 0\overset{\circ}{.}6$. The white dwarf contributes with $\simeq 25\%$ of the light at 1600 Å. If the inner disk is optically thick it has a temperature of $T_{wd} \gtrsim 65{,}000$ K. Velocity-resolved light curves in the C IV λ1550 line show evidence of rotational disturbance and a strong orbital modulation is seen in the line center light curve.

Maximum-entropy eclipse mapping techniques are used to solve for a map of the disk brightness distribution and for fluxes of an additional uneclipsed component in 18 narrow UV bands and in the *R* band. The angular scale of the disk and the distance to UX UMa are estimated from a color-magnitude diagram by a method similar to cluster main-sequence fitting. We find $D = 345 \pm 34$ pc. The radial temperature profiles derived from the UV continuum maps range from 8000 K in the outer disk regions to 30,000 K in the inner disk and reasonably follow the $T \propto R^{-3/4}$ law for steady mass accretion at a rate of $\dot{M} = 10^{-8.0\pm0.2}\ M_\odot\ \mathrm{yr}^{-1}$. The comparison of *R*-band eclipse maps from observations 2 months apart indicates changes in the structure of the outer disk which are probably due to small changes ($\lesssim 20\%$) in the mass transfer rate from the secondary star.

The maps in the C IV and He II line profiles are affected by emission from the disk wind. The radial temperature profiles of both line center maps show a flat slope. It is suggested that at low velocities the eclipsed part of the line emission arises from an opaque and extended region with a rather uniform spatial intensity distribution as projected in the plane of the sky. When plotted as a sequence of spatially resolved spectra these lines appear in absorption at disk center and change to emission in the outer disk regions besides showing large uneclipsed components. This behavior is similar to that found by Rutten et al. for the Balmer lines and suggests that these optical lines may also have a wind component.

We obtain a revised ephemeris for the times of minimum and an upper limit for secular period changes of $|\dot{P}| < 1.3 \times 10^{-12}$ s s^{-1}. The mass transfer rate inferred from this limit is an order of magnitude smaller than the value derived from the eclipse mapping, suggesting that the high mass transfer rate of UX UMa is not the consequence of its secular period decrease.

Subject headings: binaries: eclipsing — novae, cataclysmic variables — stars: individual (UX Ursae Majoris) — ultraviolet: stars

1. INTRODUCTION

Cataclysmic variables (CVs) are close interacting binaries in which a low-mass late-type star (the secondary) overflows its Roche lobe and transfers matter to a companion white dwarf (the primary). The subclass of *nova-likes* comprises systems with a high mass transfer rate ($\dot{M} \gtrsim 10^{-9}\ M_\odot\ \mathrm{yr}^{-1}$) and a white dwarf with a weak magnetic field ($B \lesssim 10^4$ G). In these systems the infalling matter forms an accretion disk which is generally the brightest luminosity source at ultraviolet (UV) and optical wavelengths. *International Ultraviolet Explorer* (*IUE*) observations show that these systems experience mass outflow in the form of high-velocity winds probably emanating from the inner disk (Cordova & Mason 1985, and references therein). Nova-likes are excellent sites for the study of accretion physics because they are easily observable at UV and optical wavelengths and also because the accretion processes occur in a relatively well understood binary environment. Eclipsing systems are particularly useful since the occultation of the accretion disk and white dwarf by the secondary star can be used to constrain the geometry and parameters of the binary and also to provide information about the disk's spatial structure.

In this paper we analyze *Hubble Space Telescope* (*HST*) time-resolved spectroscopy and ground-based photometry of the nova-like UX UMa during eclipse. The spectroscopic data were obtained with the Goddard High Resolution Spectrograph on *HST* during 1993 January 19 and 22. The combination of high spectral resolution and high time resolution

[1] Based on observations with the NASA/ESA *Hubble Space Telescope*, obtained at the Space Telescope Science Institute, which is operated by the Association of Universities for Research in Astronomy, Inc., under NASA contract NAS 5-26555.

[2] Space Telescope Science Institute, 3700 San Martin Drive, Baltimore, MD 21218; bap@stsci.edu.

[3] University of Utrecht, P.O. Box 80,000, NL-3508 TA, The Netherlands; horne@fys.ruu.nl.

[4] University of St. Andrews, North Haugh, St. Andrews, Fife KY16 9SS, Scotland, UK; kdh1@st-andrews.ac.uk, rwh@st-andrews.ac.uk.

[5] Mullard Space Science Laboratory, Holmbury St. Mary, Dorking, Surrey, RH5 6NT, England, UK; kom@mssl.ucl.ac.uk.

[6] Department of Physics, Nuclear Physics Laboratory, Keble Road, Oxford OX1 3RH, England, UK; j.drew1@physics.oxford.ac.uk.

achieved by this instrumental set gives an excellent opportunity to perform a detailed study of the emission lines and adjacent continuum, and to obtain their spatial distribution in the system. A qualitative assessment of the impact of this data set and a preliminary comparison with models were presented by Mason et al. (1995). A detailed analysis of line profile variations through eclipse will be reported in a later paper (Knigge et al. 1995). Here we concentrate mainly on the analysis of the continuum light curves. In § 3.1 we use new eclipse timings to obtain a revised ephemeris for the times of minimum and an upper limit for secular period changes. In § 3.2 we use the steep UV eclipse light curves to measure white dwarf contact phases and to revise the binary parameters. In § 3.4 we use eclipse mapping techniques to obtain maps of the eclipsed regions in a set of wavelength ranges. The results enable a close inspection of the accretion disk emission properties and are used also to estimate the distance to the binary. In § 4 we discuss the reliability of the derived binary parameters and compare the inferred mass transfer rate from the limit on secular evolution with that from the eclipse mapping. A summary of the results is presented in § 5.

2. OBSERVATIONS

2.1. HST *Time-resolved Spectroscopy*

UX UMa was observed by the Goddard High Resolution Spectrograph on *HST* during 1993 January 19 and 22. The observations consist of a series of exposures in the "rapid readout" mode using the Large Science Aperture and the G160M grating (spectral coverage $\simeq 35$ Å, $\Delta\lambda \simeq 0.07$ Å pixel^{-1}), with a time resolution of 5 s and a dead-time between exposures of 0.002 s. The adopted procedure consisted in acquiring a short run at about orbital phase 0.6 followed by a longer run covering the next eclipse. Four pairs of such runs were obtained, three of them covering the C IV λ1550 region and the last one centered in the He II λ1640 line. The observations are summarized in Table 1.

The data were subjected to the standard reduction procedures routinely performed at the Space Telescope Science Institute, which includes flat-fielding corrections, background subtraction, wavelength, and absolute flux calibrations.

Figure 1 displays average out-of-eclipse and mid-eclipse spectra, where the Si II $\lambda\lambda$1527, 1533, and the C IV $\lambda\lambda$1548, 1551 doublets as well as the He II λ1640 line can be seen. The C IV and He II lines show absorption features superimposed on broad emission profiles. At mid-eclipse phases the continuum flux is greatly reduced while the flux at C IV and He II show a rather smaller decrease, as previously seen by Holm, Panek, & Schiffer (1982) and King et al. (1983). This indicates that a substantial fraction of the flux at these wavelengths remains unocculted during eclipse. Average light curves in the continuum and in the C IV λ1550 region are illustrated below in Figures 3 and 4. These will be described in detail in §§ 2.3 and 2.4. Because of limitations imposed by the spacecraft orbit the runs have a quite restricted phase coverage, though without compromising the eclipse shape itself.

2.2. *Optical Photometry*

Optical photometry of UX UMa was obtained simultaneously with the ultraviolet spectroscopy. We used a Wright Instruments CCD camera (1".76 pixel^{-1}, 385 × 578 pixels) attached to the 0.9 m James Gregory Telescope of the University Observatory, St. Andrews, to obtain time series of differential photometry in the *R*-band (Bessell 1983). This pixel size is matched to the seeing at this sea-level site, where typical stellar images have FWHM values of 3.0 pixels, and are therefore well sampled. An exposure time of 50 s was adopted. The first run (R1) yielded simultaneous coverage with *HST* run 4. Run R2 is simultaneous with *HST* run 8. UX UMa was further observed with the same telescope and instrument configuration on 1993 March 24/25. This latter data set comprises four eclipses and two complete orbital cycles. Details are listed in Table 1. Column (7) describes the quality of the nights for the ground-based observations.

Bias subtraction and flat-fielding of the CCD frames were performed via standard FIGARO routines (Shortridge 1987). Photometry was obtained with the automated aperture photometry routine JGTPHOT (Bell, Hilditch, & Edwin 1993). Fluxes were extracted for the variable and for three selected comparison stars in the field. The relative brightness of the comparison stars in all data sets is constant to better than 0.01 mag. We adopted a mean comparison star magnitude for each frame from the intensity-added values of these three stars. Time series were constructed by computing the magnitude difference between the variable and the mean comparison star.

TABLE 1

JOURNAL OF OBSERVATIONS

Date (1993) (1)	Run Number (2)	UT Start (3)	UT End (3)	Phase Range (cycles) (4)	Number of Exposures (5)	Wavelength Range (Å) (6)	Q (7)
Jan 19.....	1	17:41	17:58	−0.40, −0.34	198	1538–1573	
	2	19:00	19:46	−0.13, +0.04	562	1538–1573	
	3	22:29	22:45	−0.38, −0.32	197	1521–1556	
	4	23:49	0:36	−0.11, +0.06	562	1521–1556	
	R1	22:36	1:02	−0.37, +0.15	95	*R*-band	C
Jan 22.....	5	16:25	16:41	−0.41, −0.35	197	1521–1556	
	6	17:47	18:34	−0.13, +0.04	559	1521–1556	
	7	21:12	21:28	−0.40, −0.34	194	1619–1654	
	8	22:32	23:19	−0.12, +0.04	559	1619–1654	
	R2	22:10	2:53	−0.21, +0.79	235	*R*-band	B
Mar 24.....	R3	21:38	3:45	−0.16, +1.14	280	*R*-band	A
Mar 25.....	R4	21:18	3:33	−0.15, +1.18	280	*R*-band	A

NOTES.—A = photometric; B = good; C = fair.

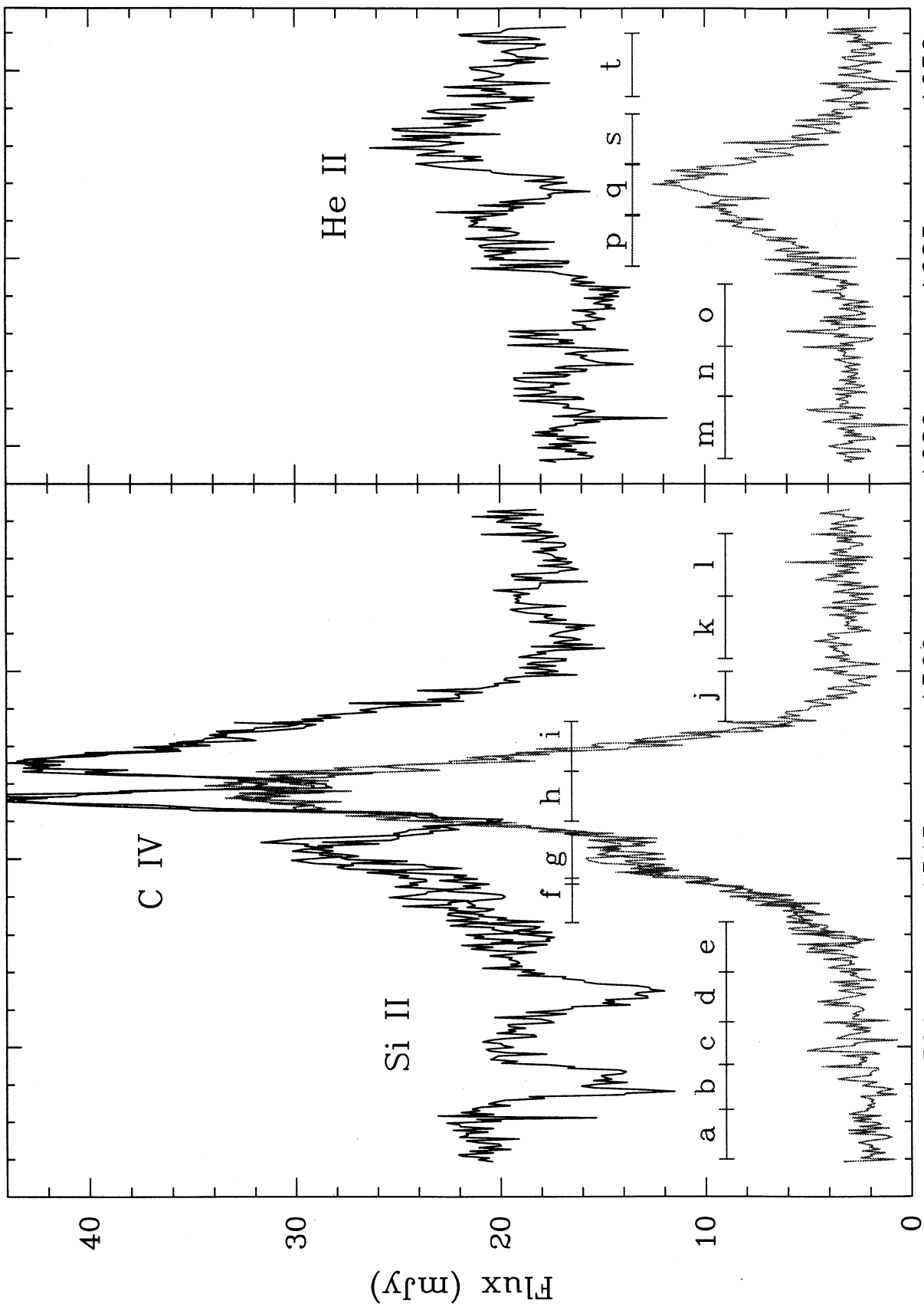

FIG. 1.—Average out-of-eclipse (in black, phase range −0.12 to −0.04 cycles) and mid-eclipse (in light gray, from −0.02 to +0.02 cycles) spectra of UX UMa in the C IV λ1550 and He II λ1640 regions on 1993 January 19/22. The 18 narrow-wavelength ranges used to extract eclipse light curves are labeled.

From the dispersion in the magnitude difference of comparison stars with similar brightness we estimate an uncertainty of 0.01 mag in the photometry of UX UMa.

Observations of *VRI* equatorial standard stars of Landolt (1983) and of spectrophotometric standard stars of Massey et al. (1988) were used to calibrate the *R*-photometry in the UX UMa field. These observations demonstrate that the transformation coefficients from the natural to the standard *VRI* system (Bessell 1983) are unity to a precision of 1%. Hence differential instrumental magnitudes obtained from individual frames are differential *V*, *R*, and *I* magnitudes. We found a mean combined magnitude of the three comparison stars of $R = 11.79 \pm 0.04$ mag. We used the relation $R = 16.22 - 2.5 \log_{10} f_\nu$(mJy) (Lamla 1981) to transform the calibrated magnitudes to absolute flux units.

2.3. *Continuum Light Curves*

We adopted the following convention regarding the phases: conjunction occurs at phase zero, the phases are negative before conjunction and positive after conjunction. The light curves were phased according to the linear ephemeris derived in § 3.1. A phase correction of −0.003 cycles was further applied to the data to make the center of the white dwarf eclipse coincident with phase zero (see § 3.2).

Figure 2 shows average *R*-band orbital light curves for the January and March observations as well as the difference between the two light curves. Contemporary observations made with *IUE* show that, at the time of the *HST* observations, UX UMa was fainter in comparison to the average *IUE* archive spectrum (Mason et al. 1995; see their Fig. 2). The corresponding *R*-band light curve has a rather constant level outside of the eclipse (at $R = 12.9$) with only minor evidence of an orbital hump at orbital phase $\simeq -0.1$. The eclipse shape is typical of the optical behavior of this system (e.g., Warner & Nather 1972), showing a smooth profile with a noticeable asymmetry in the egress—the signature of a bright spot that forms at the intersection of the inflowing stream of matter with the edge of the disk. UX UMa was brighter ($R \simeq 12.8$) during the March observations. In comparison with the January light curve, the orbital hump appears more pronounced (with an

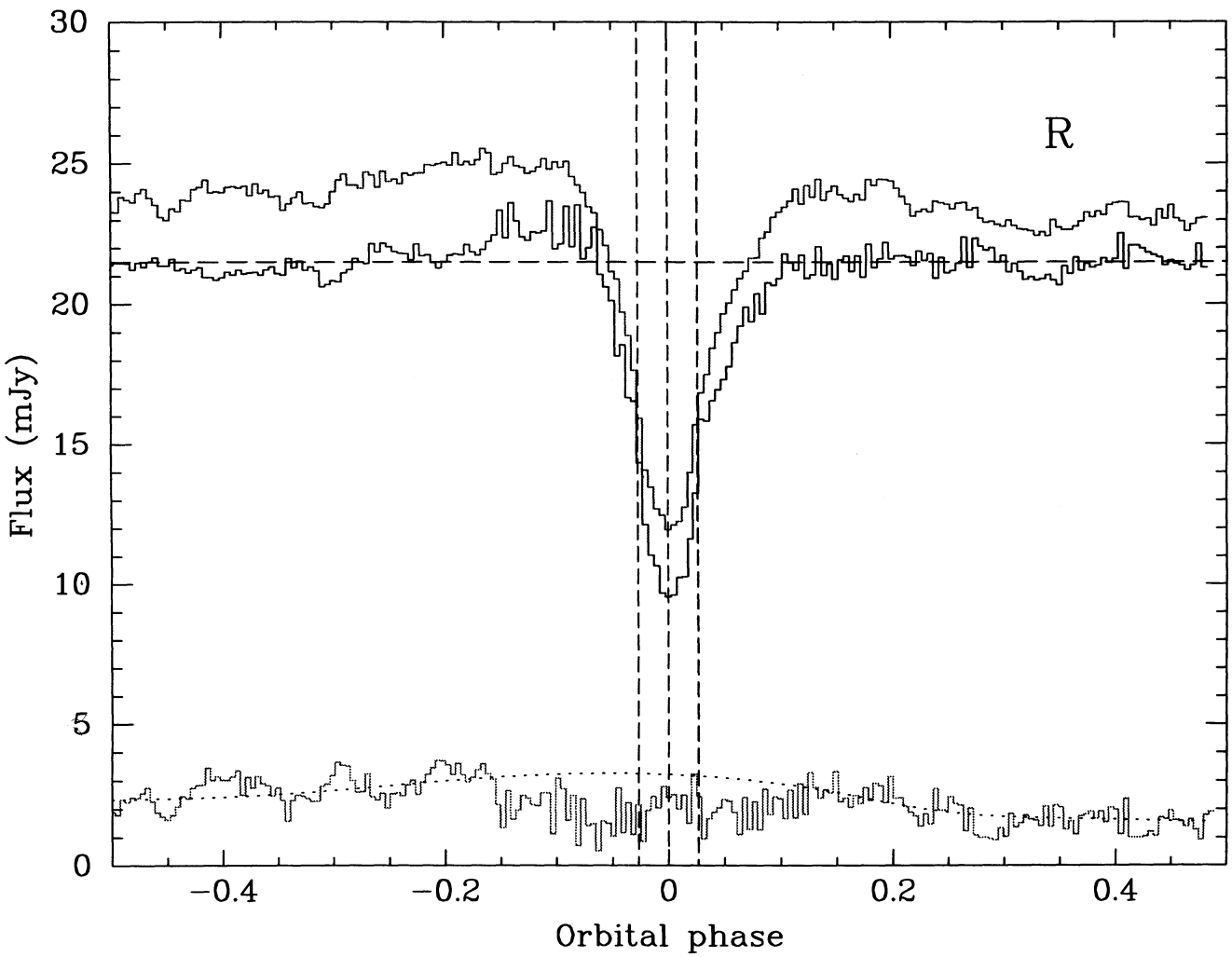

FIG. 2.—Average orbital light curves in the *R*-band for the January 19/22 (black) and March 24/25 (gray) observations. The data were phase-binned to a resolution of 0.005 cycles. The lower curve (in light gray) shows the difference (in the sense March minus January) of the above orbital curves as a function of phase. The dotted line is a spline fit to the out-of-eclipse regions of this curve. Dashed vertical lines mark mid eclipse phase and ingress/egress phases of the white dwarf. A horizontal dashed line depicts the average out-of-eclipse level for the January observations.

amplitude of $\simeq 10\%$), the flux at mid-eclipse has increased in proportion to the out-of-eclipse brightening, and the eclipse has a larger width at zero depth. The light curve of the difference (in the sense March minus January) shows evidence of a shallow eclipse and of a broad orbital hump with maximum at phase $\simeq -0.05$. These remarks suggests that the disk radius was larger in March and that the source responsible for the brightness increase remains largely unocculted at mid-eclipse phases.

The ultraviolet light curves in Figure 3 show marked differences with respect to the *R*-band light curves in Figure 2. The UV eclipses are deep, nearly reaching the zero level at mid-eclipse phases. Sharp ingress and egress features reveal the occultation of the white dwarf at disk center. The eclipse width at zero depth is much smaller in this case indicating that the UV light is more centrally concentrated than the *R* light, consistent with the existence of a temperature gradient in the accretion disk, the temperature being lower in the outer disk regions. There is almost no evidence of the orbital hump or of the bright spot. The contemporary eclipse map in the *R*-band indicates that the bright spot had a temperature of $\sim 10^4$ K (see Fig. 11 below). If we assume blackbody radiation, it is straightforward to show that at ~ 1550 Å the spectrum is well beyond the Wien cutoff frequency and no significant emission should be expected.

2.4. C IV *Light Curves*

Figure 4 shows average velocity-resolved eclipse light curves in the C IV $\lambda 1550$ line. The light curve in each wavelength bin is shown along with a continuum light curve for comparison. The wavelength ranges used to extract these light curves are shown in Figure 1. We mention that each light curve includes the total flux at the corresponding wavelength range, i.e., there is no subtraction of an interpolated continuum contribution. The observed eclipse shapes and out-of-eclipse modulations are consistent in the sense that the same general behavior is observed in all individual light curves—which were obtained in different nights—used to compute these averages. While the UV continuum eclipses are deep and almost total, the C IV velocity-resolved eclipse light curves are partial and become increasingly shallow toward the line center. Curves *f* and *g* (blue wing of C IV) show a minimum slightly before phase zero, while in the light curves *i* and possibly *j* (red wing of C IV) the eclipse minimum occurs after phase zero. This suggests that the

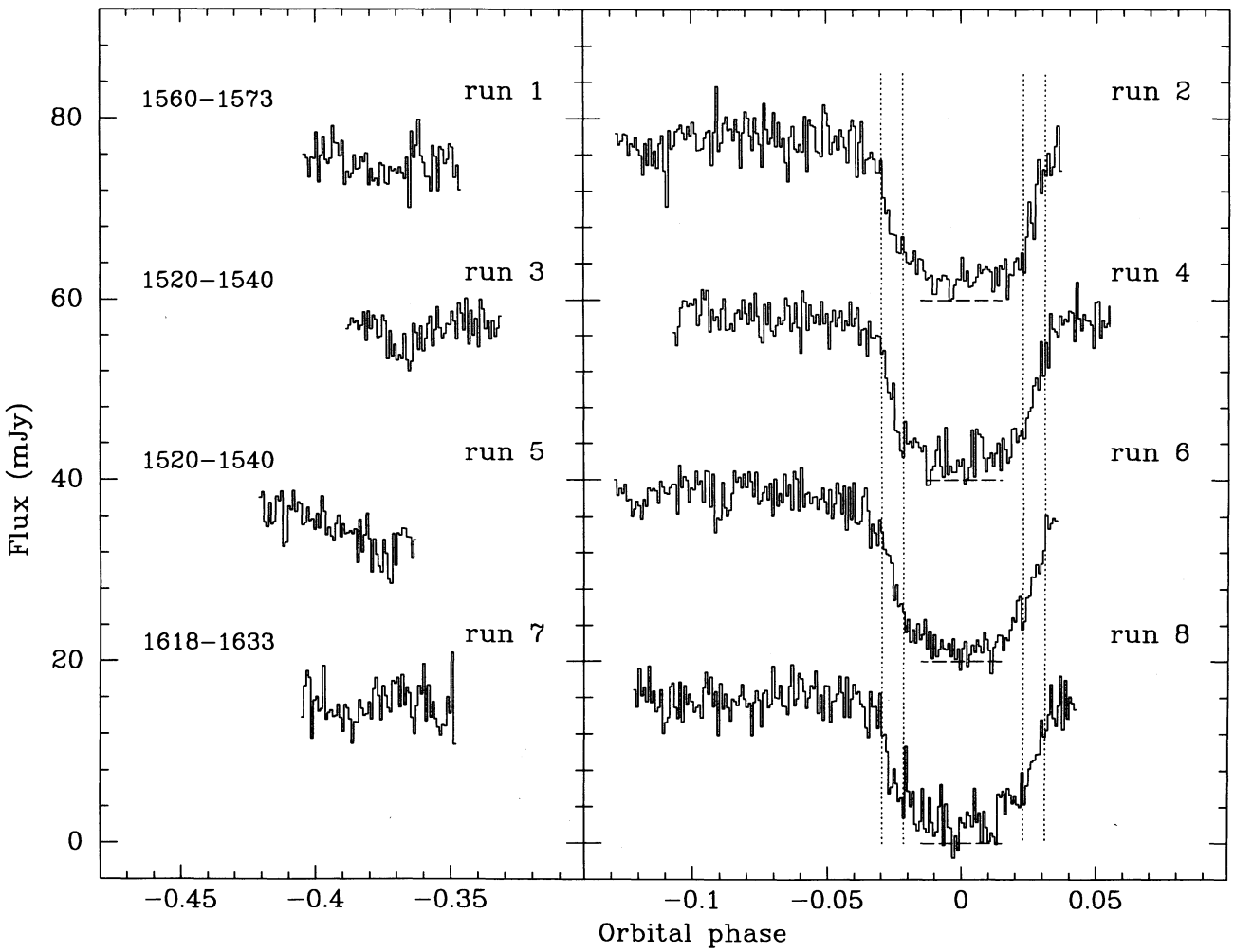

FIG. 3.—*HST* continuum light curves. Wavelength ranges are marked in the left. The light curves were phased according to the ephemeris of eq. (1) and further corrected by -0.003 cycles to center the eclipse on the white dwarf (§ 3.2). Vertical dotted lines show the contact phases of the white dwarf as measured in § 3.2. The curves are progressively displaced upward by 20 mJy. Dashed lines at mid-eclipse show the true zero level in each case.

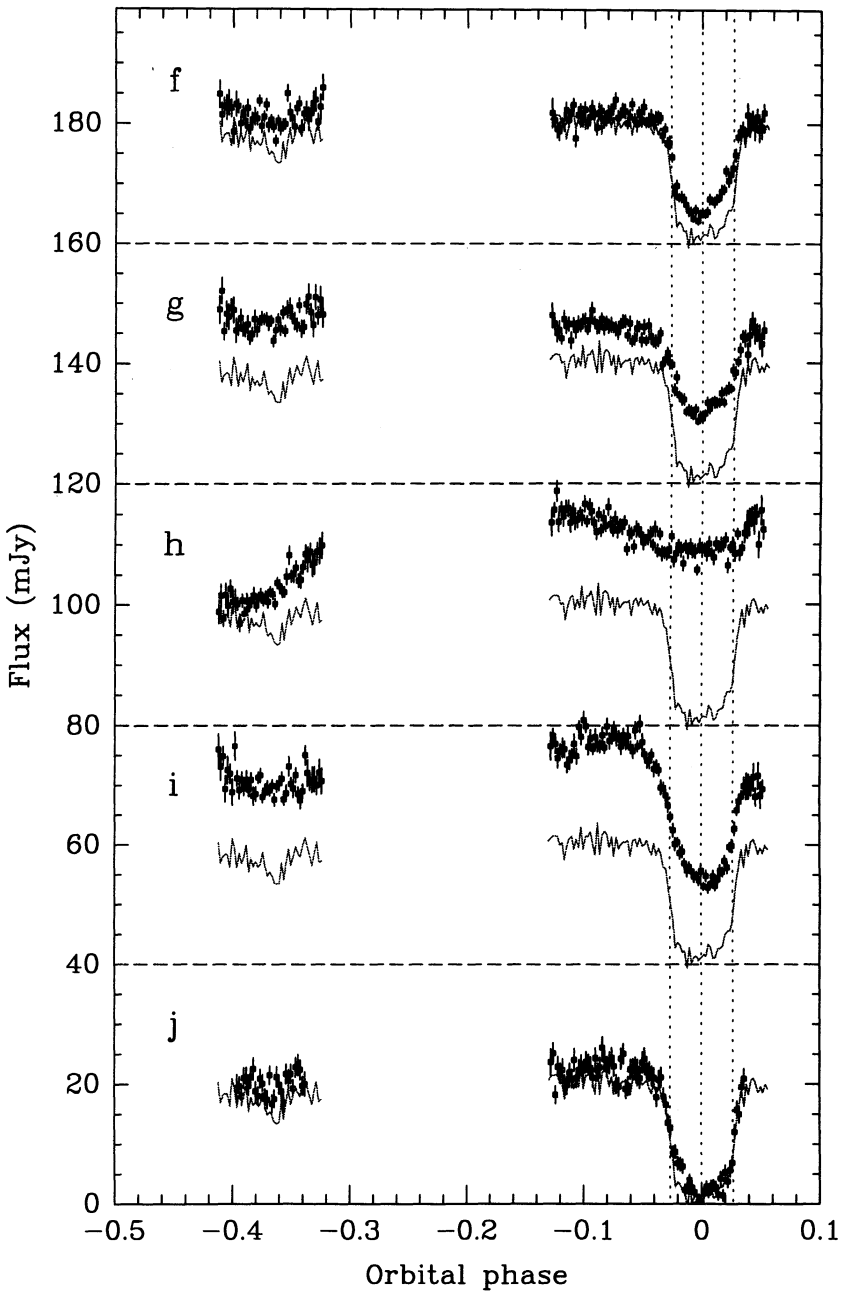

FIG. 4.—Light curves at selected wavelength ranges around C IV λ1550 (see Fig. 1), binned to a phase resolution of 0.002 cycles. Vertical bars show the uncertainties at each phase. The curves are progressively displaced upward by 40 mJy. Dashed lines show the true zero level in each case. Dotted lines mark mid-eclipse phase and ingress/egress phases of the white dwarf. The average light curve of the continuum wavelength range *a* is plotted as a solid curve in each panel for comparison.

blue wing emission has an asymmetric distribution in the approaching side of the disk and that the red wing shows a similar asymmetry in the receding side of the disk—an evidence of rotational disturbance in this line. Light curves *f*, *g*, and *i* show two sharp features in the eclipse, which coincide with the ingress/egress of the white dwarf as measured in § 3.2.

The C IV velocity-resolved light curves also show significant differences with respect to the continuum light curves outside of the eclipse. Light curve *i* displays a notable orbital hump (amplitude $\simeq 20\%$) which is not seen in its blue equivalent, curve *g*, nor in the continuum. It is also noteworthy that the line center curve *h* shows a conspicuous orbital modulation with an apparent amplitude of $\simeq 50\%$ and that the flux at mid-eclipse is higher than that at phase -0.4. This behavior may be reminiscent of the orbital phase linked variations in the UV observed in low-inclination systems (Knigge et al. 1994 and references therein). Figure 4 gives the time (or phase) view of this effect in UX UMa. The reader is referred to Mason et al. (1994) for a description of this orbital behavior in terms of its corresponding spectral changes. These observations suggest either that the C IV λ1550 line has velocity-dependent anisotropic emission (the anisotropy being stronger at lower veloci-

ties and for redshifted emission), or that significant absorption occurs at orbital phase ~0.5 where the secondary star and the bright spot region are behind the disk and its extended atmosphere.

A further inference can be made with a simple comparison of the shapes of the continuum and C IV line center light curves. Let us consider three possible scenarios: (1) the line and continuum emission are produced in separated regions in such a way that the radiation patterns toward the observer do not interfere with each other; (2) the continuum light passes through the line-forming region before reaching the observer and the line-emitting region is optically thin; and (3) the same as case (2) but the line emitting region is optically thick. In cases (1) and (2) the observed light is simply the sum of the contributions from the continuum and line emitting regions. Hence, an eclipse light curve should show a similar break/jump in slope as observed in the adjacent continuum during ingress/egress. On the other hand, in case (3)—since the intervening line emitting gas is opaque—the background continuum cannot be seen and the eclipse shape is given by the brightness distribution (and size) of the opaque veiling gas. The eclipse in light curve *h* is perceptibly wider and much shallower than that of the continuum curve *a*. Furthermore, there is no significant break or jump in the slope of the curve at the ingress/egress phases of the white dwarf—which correspond to dramatic changes in the flux of the continuum curve. These remarks and the above reasoning strongly suggest that the eclipsed part of the line emission at the wavelength range *h* is optically thick and comes from a region more extended than the continuum-forming region (the accretion disk). In the spirit of this interpretation, it makes no sense to subtract a continuum contribution from bin *h* before constructing the light curve. The observed increase in the *net emission* line flux during eclipse (Mason et al. 1995) is then due to the fact that, during this time, the continuum adjacent to C IV practically disappears behind the shadow of the secondary star while the line center emission suffers only a minor reduction due to a partial occultation of the (opaque) extended source. A similar inference can be drawn for the He II line center emission.

3. RESULTS

3.1. *Revised Ephemeris and Upper Limit for Orbital Period Changes*

In this section we use eclipse timings measured from our data together with timings previously published in the literature to compute a revised ephemeris for the eclipses of UX UMa.

Eclipse timings were measured (1) by fitting parabolic and cubic functions to the eclipse data to estimate *times of minimum*; and (2) by using variations of the bisected chord method to obtain *mid-eclipse times* (Baptista, Jablonski, & Steiner 1989). For the case of the *HST* continuum light curves, which present fairly steep ingress/egress features, we also estimated eclipse timings by computing the phases of maximum and minimum derivative in the light curves (§ 3.2)—the midpoint of these two phases gives an estimate of the mid-eclipse time. The final timing is the average of the measurements from all methods used. Times of minimum tend to be later than mid-eclipse timings in UX UMa, however the differences are much smaller than the uncertainties adopted for the following analysis. We also used the above procedures to measure an eclipse timing from the *Hopkins Ultraviolet Telescope* observations of UX UMa (R. Baptista & K. Long 1994, private communication), corresponding to eclipse cycle 22014. The new heliocentric (HJD) timings of UX UMa are listed in Table 2. For the eclipses with simultaneous *HST* and ground-based coverage the quoted time is the average of both estimates.

TABLE 2

NEW ECLIPSE TIMINGS OF URSAE MAJORIS

E	HJD (2,440,000 +)	O − C[a] (cycles)
22014.....	8234.4009	+0.0036
25944.....	9007.3187	+0.0018
25945.....	9007.5154	+0.0020
25959.....	9010.2692	+0.0040
25960.....	9010.4657	+0.0031
26270.....	9071.4330	−0.0007
26271.....	9071.6300	+0.0009
26275.....	9072.4164	−0.0006
26276.....	9072.6132	+0.0001

[a] Observed minus calculated times with respect to the ephemeris of eq. (1).

For the analysis we included the timings of Nather & Robinson (1974), Africano & Wilson (1976), Kukarkin (1977), Quigley & Africano (1978), Rubenstein, Patterson, & Africano (1991), and Rutten, van Paradijs, & Tinbergen (1992). Three of the visual timings of Kukarkin (1977) and one of the timings of Nather & Robinson (1974) were excluded as they deviate from the distribution by more than 5 minutes (≃0.022 cycles).

We obtained least-squares linear and parabolic fits to the combined data set by assuming (1) equal errors of $0^d.0004$ for all measurements (unweighted fit); and (2) uncertainties of $0^d.0002$ for the photoelectric timings and $0^d.0003$ for the visual timings (weighted fit). For the linear fit, the weighted and unweighted ephemerides are identical within the errors. The best-fit linear ephemeris (with 1 σ errors) is

$$T_{\min} = \text{HJD } 2\,443\,904.878\,72(\pm 3) + 0.196\,671\,278(\pm 2)E\,, \quad (1)$$

where E is the cycle number. The covariance between the parameters of the fit is $+1.7 \times 10^{-15}$ d^2. $O - C$ values with respect to this ephemeris are listed in Table 2 and plotted in Figure 5.

The significance of the parabolic fit depends on the weights given to individual timings. The unweighted fit yields a quadratic coefficient of $(-1.1 \pm 0.4) \times 10^{-13}$ d. This ephemeris is shown as a solid line in Figure 5. The significance of adding an additional term to the linear ephemeris was calculated following the prescription of Pringle (1975). The *F*-test indicates that the quadratic term is significant at the 82% level, considerably lower than the 93.2% value previously found by Rubenstein et al. (1991). The quadratic term is largely dominated by the first visual measurements. The weighted fit—which reduces the influence of the visual measurements in determining the ephemeris—results in a coefficient of $(+0.4 \pm 0.4) \times 10^{-13}$ d. Thus, we conclude that there is yet no evidence of secular orbital period change in UX UMa. From the 3 σ value of the error in the quadratic coefficient above, we obtain an upper limit for orbital period variations of

$$|\dot{P}| < 1.3 \times 10^{-12} \text{ s s}^{-1}\,, \quad P_0/|\dot{P}| > 4.1 \times 10^8 \text{ yr}\,. \quad (2)$$

3.2. *Revised Binary Parameters*

The ultraviolet light curves of Figure 3 allow a close inspection of the white dwarf in UX UMa for the first time—this

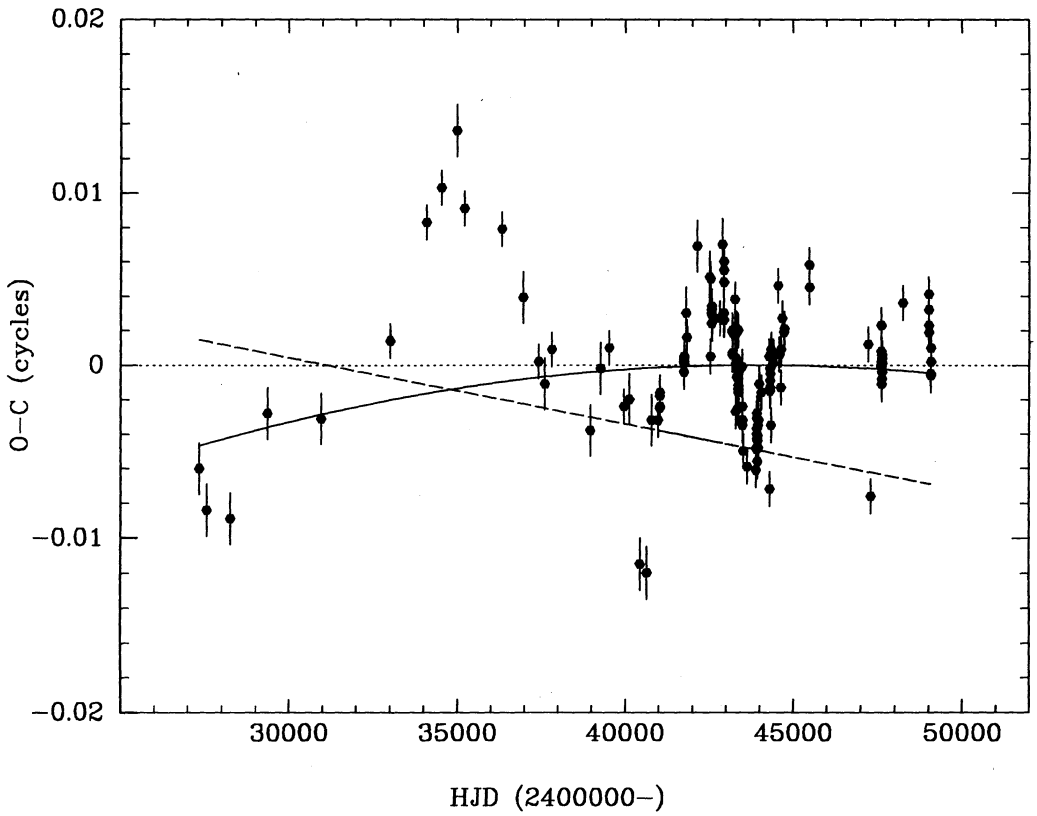

FIG. 5.—The $O - C$ diagram for the eclipse timings with respect to the ephemeris in eq. (1). A dashed line shows the ephemeris of Rubenstein et al. (1991). The solid line is the best-fit unweighted parabolic ephemeris.

compact blue object cannot be distinguished in optical light curves (e.g., Fig. 2). In this section we use the ultraviolet eclipse contact phases of the white dwarf to constrain the geometry of the system and to revise the binary parameters.

We combined the continuum eclipse light curves in Figure 3 to obtain an average light curve with increased signal-to-noise ratio (Fig. 6). Contact phases were measured with the aid of a cursor on a graphic display and by means of the derivative technique described by Wood, Irwin, & Pringle (1985). This latter technique is illustrated in Figure 6. The average light curve (Fig. 6*a*) is smoothed with a median filter of width 0.0025 cycles (Fig. 6*b*) and its numerical derivative is computed. The amount of filtering used at this point is a compromise between the aim to suppress noise in the light curve as much as possible and the need to preserve any real structures in the eclipse shape. The ingress/egress of the white dwarf are seen as those intervals for which the derivative curve is significantly different from zero. The width at half-peak intensity of these features yields a preliminary estimate of their duration. A spline function is fitted to the remaining regions in the derivative curve to remove the contribution from the extended and slowly varying eclipse of the disk. The spline-subtracted derivative curve (Fig. 6*c*) is then analyzed by an algorithm which identifies the points of extrema (the mid-ingress/egress phases ϕ_{wi}, ϕ_{we}) and the points where the derivative starts to depart from the zero-constant level (the contact points ϕ_{w1-4}). A median filter of equal width to that used in the first part of the reduction is applied to the derivative curve to aid in the detection. The same procedures were used to measure contact phases from the individual light curves in Figure 3.

The duration of the eclipse of the white dwarf is defined as

$$\Delta\phi = \phi_{we} - \phi_{wi} , \tag{3}$$

and the center of the white dwarf eclipse (the inferior conjunction of the binary) is written as

$$\phi_0 = \tfrac{1}{2}(\phi_{we} + \phi_{wi}) . \tag{4}$$

The median of the measurements from all light curves yields $\Delta\phi = 0.053 \pm 0.001$ cycles, where the quoted error is the median of the absolute deviations with respect to the median. Similarly, we have $\phi_0 = +0.003 \pm 0.001$ cycles.

The measured value of $\Delta\phi$ can be used to set a unique relation between the mass ratio q and the inclination i of the binary (Bailey 1979; Horne 1985). We assumed that the shape of the secondary star is given by the Roche equipotential surface and used a Newton-Raphson algorithm (Press et al. 1986) to compute the numerical relationship $i = i(q, \Delta\phi)$. For the measured $\Delta\phi$, a value of $q = 1.0$ (see below) corresponds to $i = 71\overset{\circ}{.}0$.

The mean phase width of the white dwarf ingress and egress features is

$$\Delta\phi_{wd} = \tfrac{1}{2}[(\phi_{w2} - \phi_{w1}) + (\phi_{w4} - \phi_{w3})] . \tag{5}$$

A median from all measured contact phases gives $\Delta\phi_{wd} = 0.008 \pm 0.001$ cycles. An estimate of the diameter of the white dwarf can be obtained from the duration of its ingress/egress feature in the eclipse light curve. These quantities are related by the approximate relations (Ritter 1980),

$$2R_1 \simeq 2\pi\,\Delta\phi_{wd}\, z(q) a \sin\theta , \tag{6}$$

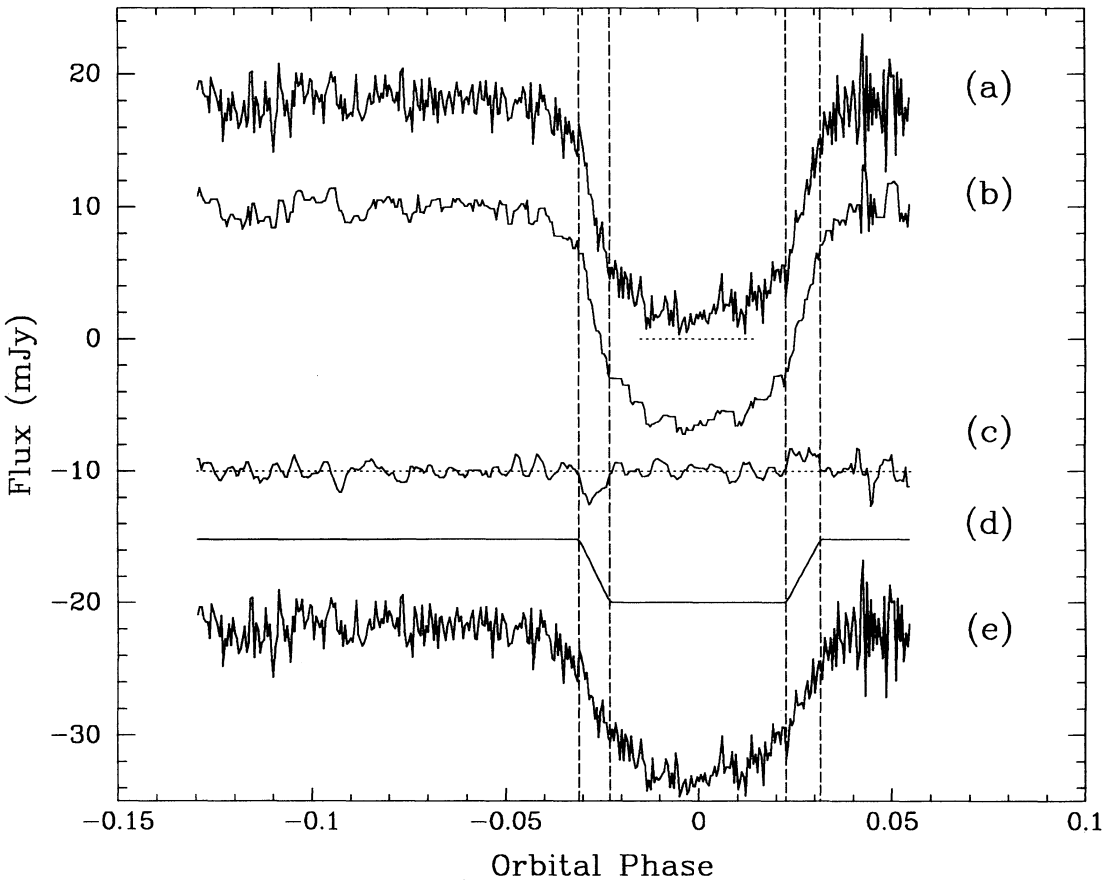

FIG. 6.—Extracting contact phases from the average continuum light curve. (*a*) Combined continuum light curve from runs 2, 4, 6, and 8, binned to a phase resolution of 0.0005 cycles. (*b*) Median-filtered light curve, shifted downward by 8 mJy. (*c*) The derivative of light curve (*b*) after removing the slowly varying disk component, shifted downward by 10 mJy and multiplied by a factor 5. (*d*) The reconstructed white dwarf light curve, shifted downwards by 20 mJy. (*e*) The light curve without the white dwarf component, shifted downward by 35 mJy. Dashed lines mark the four white dwarf contact phases.

and

$$\cos\theta \simeq \frac{a}{R_2}\cos i\,, \tag{7}$$

where R_1 and R_2 are, respectively, the radius of the white dwarf and of the secondary star, a is the orbital separation, and $z(q)$ is a slowly varying function usually close to unity (Baptista et al. 1989). For the eclipse duration $\Delta\phi_{wd}$ of UX UMa, $q = 1.0$ corresponds to $z = 0.907$. The error introduced by the use of equation (6) is of order of $(R_1/R_2)^2$ and thus much smaller than the uncertainties affecting $\Delta\phi_{wd}$.

Equation (6) can be combined with Kepler's third law to obtain an expression relating the mass and the radius of the white dwarf in UX UMa,

$$R_1/R_\odot = 5.055\,\Delta\phi_{wd}(M_1/M_{Ch})^{1/3}f(q)\,, \tag{8}$$

where $M_{Ch} = 1.44\ M_\odot$ is the Chandrasekhar mass limit and $f(q) = z\sin\theta\,(1+q)^{1/3}$. Assuming that the white dwarf obeys the Hamada-Salpeter mass-radius relationship for cool degenerate stars (Hamada & Salpeter 1961), one can use the analytical approximation of Nauenberg (1972),

$$R_1/R_\odot = 0.0112\left[\left(\frac{M_1}{M_{Ch}}\right)^{-2/3} - \left(\frac{M_1}{M_{Ch}}\right)^{2/3}\right]^{1/2}, \tag{9}$$

to eliminate the term in $R_1/R_\odot$ and solve for $M_1(q, \Delta\phi_{wd})$. This relation, derived purely from photometric quantities, can be used to constraint the masses of the component stars.

Figure 7 shows the primary-secondary mass diagram for UX UMa. The photometric relation $M_1(q, \Delta\phi_{wd})$ appears as a steep line in the diagram. It essentially restricts the range of possible white dwarf masses. We have also plotted lines corresponding to the empirical ZAMS relation of Caillault & Patterson (1990) and the primary mass function for a radial velocity of $K_1 =$ 160 km s^{-1} (Shafter 1984). The three relations are consistent at the 1 σ level. If we assume the secondary star is on the main sequence then the photometric constraint above gives $q = 1.1$, $i = 70°.4$, and $K_1 \simeq 180$ km s^{-1} is predicted. If $K_1 = 160$ km s^{-1} is a correct estimate of the white dwarf radial motion then we have $q = 0.95$ ($i = 71°.3$), and a slightly evolved secondary star results. As a compromise between these two possibilities, we choose $q = 1.0 \pm 0.1$ as our solution. The corresponding binary parameters are listed in Table 3. The quoted errors were obtained by propagating the uncertainties in $\Delta\phi_{wd}$ and q with a Monte Carlo error propagation code.

Integrating the flux in the derivative curve Figure 6*c* between the first and second (third and fourth) contact phases we obtain estimates of the white dwarf flux at ingress (egress). The light curve of the white dwarf is then reconstructed by assuming that the flux is zero between ingress and egress and that it is constant outside eclipse. The reconstructed white dwarf light curve can be seen in Figure 6*d*, and the light curve

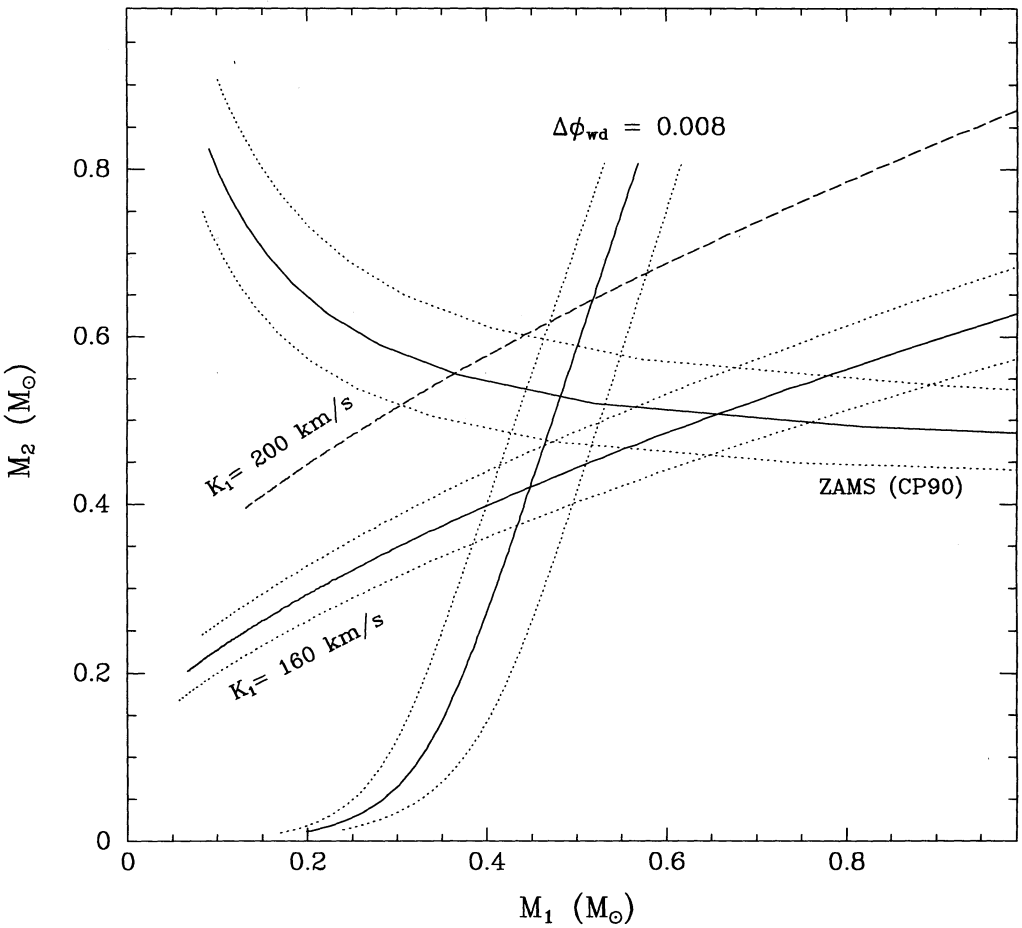

FIG. 7.—Primary-secondary mass diagram for UX UMa. Solid lines show the constraints obtained from the measured $\Delta\phi_{wd}$, the empirical ZAMS mass-radius relation of Caillault & Patterson (1990) [CP90], and the mass function for a white dwarf radial velocity of $K_1 = 160$ km s^{-1} (Shafter 1984). A dashed line shows the mass function relation for $K_1 = 200$ km s^{-1}. Dotted lines correspond to the 1 σ limit on each relation.

after removal of the white dwarf component is shown in Figure 6*e*. The average of the white dwarf fluxes at ingress and egress give $f_{wd}(1600\ \text{Å}) = 4.8 \pm 0.4$ mJy ($\simeq$25% of the out-of-eclipse flux). We have fitted white dwarf atmosphere model spectra ($\log g = 8$, solar-abundance) to the measured flux assuming a distance of 345 pc to UX UMa (§ 3.4.4) and a white dwarf radius of 0.014 $R_\odot$ (Table 3). The corresponding model temperature depends on the effective emitting area of the white dwarf as seen by an observer on Earth. If the inner disk is optically thin both white dwarf hemispheres are seen and a white dwarf temperature of $T_{wd} = 52{,}000 \pm 3000$ K is obtained. If the inner disk is opaque, the lower white dwarf hemisphere is occulted and the effective area is reduced by a factor of 2. The temperature in this case is slightly higher than that of the hottest white dwarf model available in our sample, $T = 65{,}000$ K. A blackbody fit yields $T_{wd} = 70{,}000 \pm 2000$ K. The above models predict a white dwarf flux of 0.7 mJy at 5500 Å ($\simeq$3% of the out-of-eclipse flux at this wavelength), which is consistent with the absence of white dwarf features in optical light curves of UX UMa. In both cases the inferred temperatures are within the range expected for white dwarfs in high mass-transfer CVs (Sion 1985, 1987).

Possible systematic errors affecting the measured $\Delta\phi_{wd}$ and f_{wd} values are discussed in § 4.1.

TABLE 3

ADOPTED BINARY PARAMETERS

Parameter	Value
q	1.0 ± 0.1
$M_1/M_\odot$	0.47 ± 0.07
$M_2/M_\odot$	0.47 ± 0.10
$a/R_\odot$	1.39 ± 0.08
$R_{L1}/R_\odot$	0.70 ± 0.04
i (deg)	71.0 ± 0.6
$R_1/R_\odot$	0.014 ± 0.001
$R_2/R_\odot$	0.51 ± 0.04
K_1 (km s^{-1})	170 ± 20
K_2 (km s^{-1})	169 ± 9

3.3. *Search for Oscillations*

Previous observations of UX UMa have revealed intermittent optical oscillations of amplitude 0.002 mag and with periods 28–30 s (Warner & Nather 1972; Nather & Robinson 1974). The short periods suggest that these oscillations arise in the inner disk region or boundary layer, which leads to the expectation that their amplitude may be much higher in the UV. In this section we analyze the *HST* data in search for evidence of periodic signals.

We extracted light curves for the continuum and for the C IV and He II lines (including both line emission and underlying

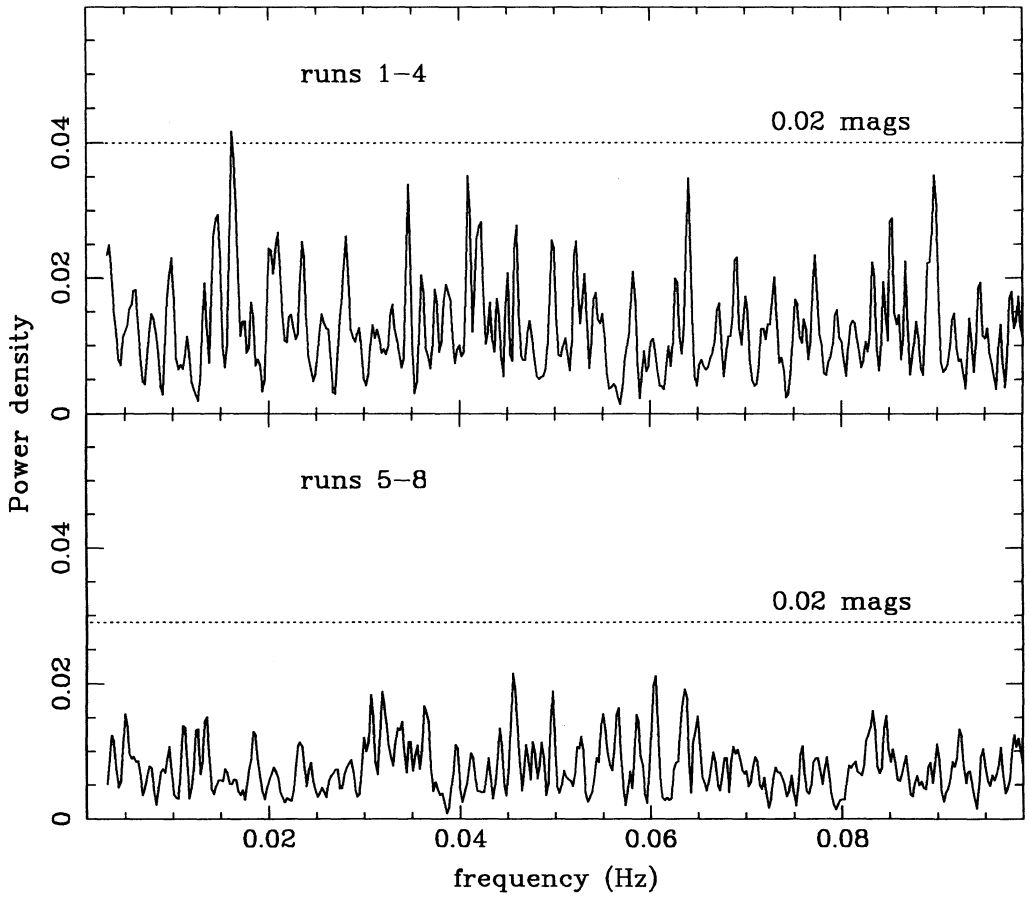

FIG. 8.—*Upper*: the power density spectrum of the combined runs 1–4 in the continuum near C IV λ1550. A dotted line shows the power level corresponding to a semi-amplitude of 2% (0.02 mags). *Lower*: similar to above, for the combined runs 5–8. All peaks have significance lower than 0.002%.

continuum) excluding data from phases −0.06 to +0.06 to avoid the eclipse and subtracting the average value of the data set to eliminate the DC component. Fast Fourier transforms were computed for each individual data set and data sets combined for each night. Amplitude levels in the power spectrum were evaluated by injecting artificial signals of known power in the time series.

No significant feature was found in any of the individual power spectra. Figure 8 shows the power density of the combined continuum time series on both nights. The power spectra are flat, and no prominent peaks are seen. None of the strongest peaks in the data of January 19 was detected in the power spectrum of January 22 and vice versa. The strongest peak in the power spectrum of Figure 8 has a statistical significance of only 0.001%. The upper limit for the semi-amplitude of any oscillation in the *HST* data in the range 0.002–0.1 Hz is 0.02 mags. Similar amplitude and significance levels were obtained from the analysis of the C IV and He II time-series data.

Longer time series and/or wider spectral coverage will be required to improve the sensitivity of the search to lower amplitude limits.

3.4. *Multiwavelength Eclipse Maps*

In this section we use the maximum-entropy eclipse mapping method of Horne (1985) to analyze the eclipse light curves of UX UMa. A brief description of the method follows. The reader is referred to Horne (1985, 1993), Baptista & Steiner (1993), and Rutten et al. (1994) for more details.

3.4.1. *Eclipse Mapping Method*

The eclipse mapping method uses eclipse light curves to obtain a two-dimensional map of the brightness distribution of the eclipsed region. The method assumes that the eclipsed light arises from an accretion disk in the orbital plane which is occulted by the Roche lobe surface of the secondary star, and that the emitted disk radiation is independent of the orbital phase. The disk region is divided in various surface elements, the intensities of which are treated as independent parameters. These intensities are iteratively adjusted to find the brightness distribution that fits the eclipse light curve within the uncertainties. The quality of the fit is checked with a consistency statistic, usually by requiring the method to achieve a unity reduced χ^2 for the model. Because the one-dimensional light curve data cannot fully constrain a two-dimensional map, additional freedom remains to optimize some map property. A maximum entropy procedure (Skilling & Bryan 1984; Skilling 1987) is used to select, among all possible solutions, the one that maximizes the entropy of the map with respect to a smooth default map. Horne (1985) showed that using an axisymmetric average of the actual map as the default map correctly reconstructs the radial structure of the map, although suppressing its azimuthal structure. When mapping accretion

disks this choice is reasonable because one expects the disk material to be roughly in Keplerian orbits, so that local departures from axisymmetry will tend to be diminished by the strong shear.

The default map with full azimuthal smearing results in rather distorted reproduction of asymmetric structures (such as a bright spot at disk edge). The reconstructions present a lower integrated flux in the asymmetric source region, the excess being redistributed as a concentric annulus about the same radial distance (see Horne 1985). The effect is more pronounced for relatively low inclination systems such as UX UMa, where a nonnegligible fraction of the far side of the disk remains uneclipsed at all phases. Since the eclipse light curve does not contain information on this disk region, the use of full azimuthal smearing results in relatively high intensities in the uneclipsed region, at the same radial distance as the bright spot. To alleviate this effect Rutten et al. (1993) introduced a default map with *limited* azimuthal smearing. By reducing the amount of azimuthal smearing this type of default map is better suited to reproduce asymmetric structures in the maps. We here follow the prescription of Rutten et al. and adopt a default map which limits the azimuthal average to a Gaussian profile of width 30°.

By studying the response of the eclipse mapping method to offsets in the zero-intensity level, Rutten et al. (1992) found that the entropy function can be a useful tool to signal and to isolate the fraction of the total light which is not coming from the accretion disk plane. They noted that when the light curve is contaminated by the presence of additional light (e.g., from the secondary star) the reconstructed map shows a spurious structure in its outermost region. This is due to the fact that the eclipse mapping method assumes all light is coming from the accretion disk: when this is true, the eclipse depth and width are correlated in the sense that a narrower shape corresponds to a deeper eclipse. The addition of an uneclipsed component in the light curve (i.e., light from a source other than the accretion disk) ruins this correlation. To account for the extra amount of light at mid-eclipse and to preserve the brightness distribution derived from the eclipse shape the algorithm inserts the additional light in the region of the map which is least affected by the eclipse. Since the entropy measures the amount of structure in the map, the presence of these spurious structures is flagged with lower entropy values. The correct offset level can often be found by comparing a set of maps obtained with different offsets and selecting the one with highest entropy. Equivalently, the value of the zero-intensity level can be included in the mapping algorithm as an additional free parameter to be fitted along with the intensity map in the search for the maximum entropy solution (see Rutten et al. 1994). Our fitting procedure includes an additional free parameter, the background flux F_{bg}, to account for the uneclipsed component. This additional parameter itself does not contribute directly to the entropy measure.

For the eclipse mapping reconstructions we use the PRIDA program (Baptista & Steiner 1991, 1993) which, aside from the usual χ^2 consistency statistic, uses the additional R-statistic to avoid the presence of correlated residuals in the model light curves. The program implements a variable χ^2 algorithm, which adjusts the aimed χ^2 value during the iteration process according to the selection made for the R-statistic (Baptista & Steiner 1993). For the case of uncorrelated normally distributed residuals, the R-statistic has a Gaussian probability distribution function with average zero and unity standard deviation. We require the program to achieve an R = 0, which is equivalent to asking for a solution with uncorrelated residuals in the model light curve.

We define the *intensity map* as a grid of $\bar{41} \times \bar{41}$ pixels centered on the primary star with side 1.6 R_{L1}, where R_{L1} is the distance from the disk center to the inner Lagrangian point. The eclipse geometry is controlled by a pair of q and i values. The mass ratio q defines the shape and the relative size of the Roche lobes. The inclination i determines the shape and extension of the shadow of the secondary star as projected onto the orbital plane. For our reconstructions we adopted the values derived in § 3.2, $q = 1$ and $i = 71°$. This combination of parameters ensures that the white dwarf is at the center of the map.

3.4.2. *Light Curves and Eclipse Maps*

The *HST* spectra were divided into a set of narrow wavelength ranges 4–5 Å wide (Fig. 1). For each of the 18 spectral bins a light curve was constructed by computing the average flux on the corresponding wavelength range and phase folding the resulting data according to the ephemeris of equation (1). The phases were further corrected by -0.003 cycles to make eclipse center coincident with the inferior conjunction of the binary (§ 3.2). The resulting light curves were phase binned to a resolution of 0.002 cycles. The standard deviation of the data at each phase bin was taken as the corresponding uncertainty. A similar procedure was applied to the R-band data in obtaining average profiles for the January and March data sets. For those spectral bins including emission lines the light curves comprise the total flux at the corresponding bin with no subtraction of a possible continuum contribution. The light curves of the wavelength ranges *f–i* include data from runs 2, 4, and 6. Those for the ranges *a–e* include data from runs 4 and 6. The individual light curves present no statistically significant differences in the eclipse shape with respect to the average. The remaining light curves (*j–t*) consist of one individual data run.

The eclipse mapping method assumes that all variations in the eclipse light curve are due to the changing occultation of the emitting region by the secondary star. Hence, out-of-eclipse brightness changes are not accounted for. The orbital hump seen in the average R-band light curves (Fig. 2) was therefore removed by fitting a low-order polynomial function to the phases outside eclipse, dividing the light curve by the fitted polynomial, and scaling the result to the polynomial value at phase zero. This procedure removes orbital variations outside eclipse with only minor effects on the eclipse shape itself. A similar procedure was applied to remove the orbital hump in the light curve i (Fig. 4) before subjecting it to the eclipse mapping algorithm.

The eclipse mapping algorithm outlined in the previous section was used to solve for a map of the disk brightness distribution and for the flux of an additional uneclipsed component in each band. The left panel in Figure 9 displays eclipse light curves for one of the UV continuum spectral bins (*a*) and for the average R-band data of January (R_J) and March (R_M). Solid lines are the models obtained by the eclipse mapping. The right panel shows the corresponding eclipse maps in a logarithmic gray scale. Both R-band maps show brightness distributions which fill most of the primary Roche lobe. The bright spot is seen as the asymmetric structure in the receding side of the disk, which appears elongated in azimuth due to the azimuthal smearing effect. In contrast, the UV continuum map shows a symmetric brightness distribution strongly concentrated toward disk center with no sign of the bright spot.

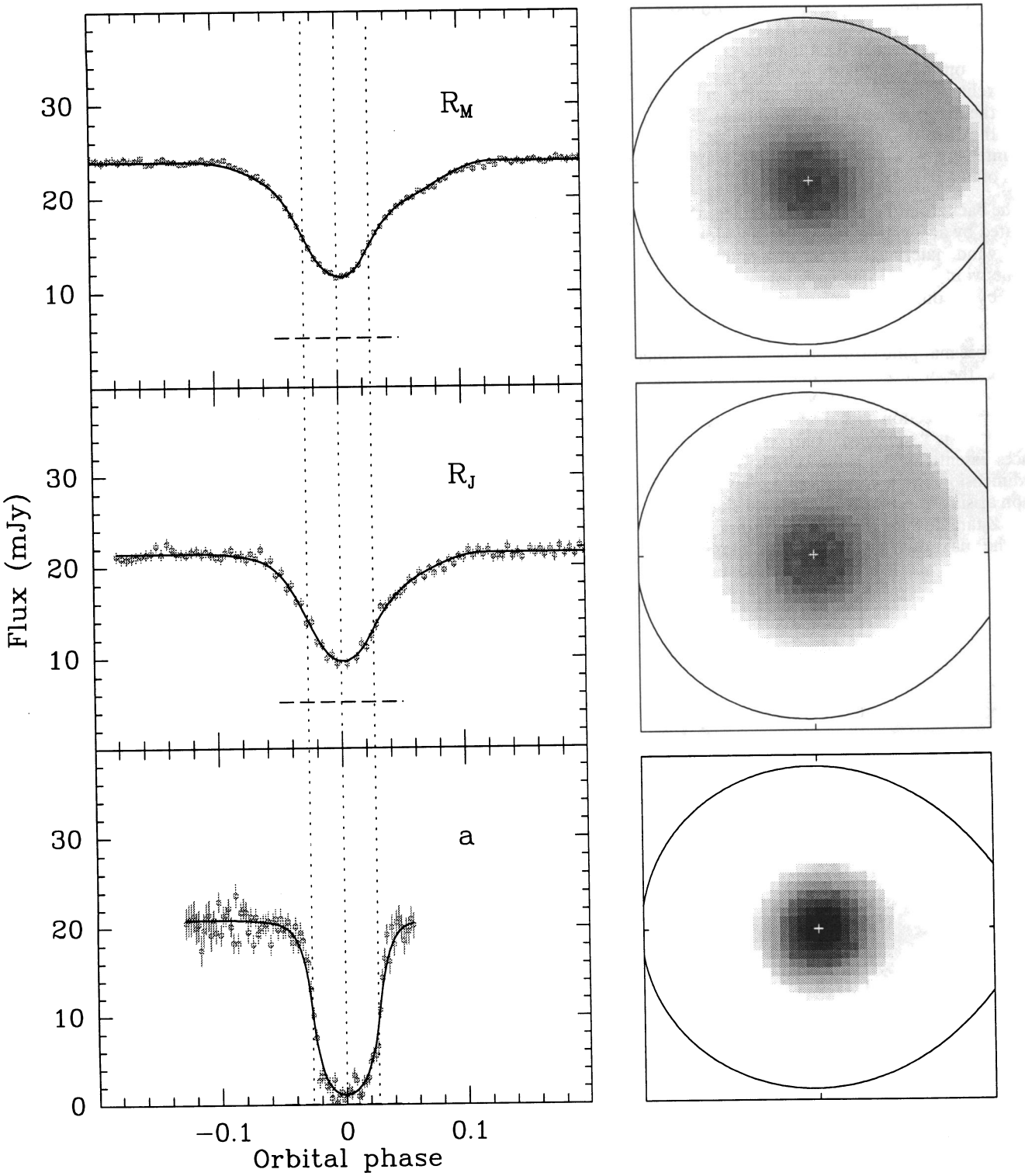

FIG. 9.—*Left*: light curves (*points*) and the fits obtained with the eclipse mapping technique (*solid curves*). Vertical bars correspond to the uncertainties at each phase. Dotted lines correspond to phase zero and to ingress/egress phases of the white dwarf. Horizontal dashed lines corresponding to the uneclipsed component are shown in each case. *Right*: Eclipse maps of the accretion disk. Dark regions are brighter. Roche lobes representing the adopted geometry are shown for reference; crosses mark the center of the disk. The secondary is to the right of each panel and the stars rotate counter-clockwise.

3.4.3. *Distortions in the Line Maps*

The P-Cygni character of the C IV and, on occasion, the He II line profiles observed in noneclipsing outburst systems combines with their large residual flux at mid-eclipse phases to indicate that they form, at least in part, in a vertically extended disk wind from near the compact object. Thus, our disk maps are not reliable for wavelengths in the emission-line profile because the mapping assumes a brightness distribution on the plane of the disk.

The intensity on a given line of sight may be considered as the sum of two parts:

1. The background emission, arising near the disk plane, but attenuated by absorption and scattering along the line of sight through wind material above the disk plane.
2. The wind-formed line emission, produced along the line of sight by a combination of thermal emission and resonant scattering.

The eclipse mapping procedure has the approximate effect of projecting the wind-formed line emission back along the inclined line of sight to the point where it pierces the disk plane. This projection yields an "equivalent" intensity distribution that is "squashed" onto the disk plane, and which produces essentially the same eclipse light curve as the real three-dimensional line-formation region. The effect is that emission arising at height Z above the disk plane is projected a distance $Z \tan i$ toward the back of the disk (cf. Fig. 11 of Drew 1987). The maximum entropy eclipse mapping method then introduces a further distortion because the intensity distribution is smeared in the azimuthal direction. The result can be quite misleading. For example, wind emission formed directly above the white dwarf can be projected toward the back edge of the disk, then smeared in azimuth to give the appearance of a broad asymmetric intensity distribution in the back side of the disk. Thus it is quite dangerous to interpret these maps literally without careful consideration of these distorting effects.

It is worth noting that, if the wind is optically thick, no information about the parts of the disk along sightlines that first pass through the opaque wind can be inferred.

We shall bear this in mind when discussing the eclipse maps at the wavelengths affected by the wind emission. The evaluation of this distortion effect and the possible interpretation of the velocity-resolved maps in the C IV and He II lines is outside the scope of the present paper.

3.4.4. *Color-Magnitude Diagram and Distance*

A color-magnitude diagram for the accretion disk in UX UMa is shown in Figure 10. The surface brightness of each pixel at 1523 Å is plotted against a temperature-sensitive UV-to-optical color index. The AB magnitudes are computed from the relation $AB(\lambda) = 16.4 - 2.5 \log_{10}[f_\nu(\mathrm{mJy})]$. This diagram differs from a classical color-magnitude diagram because the pixels in the disk map subtend identical solid angles while the stars in a cluster do not. Large dots represent pixels inside radius $0.3R_{L1}$, while the small dots correspond to

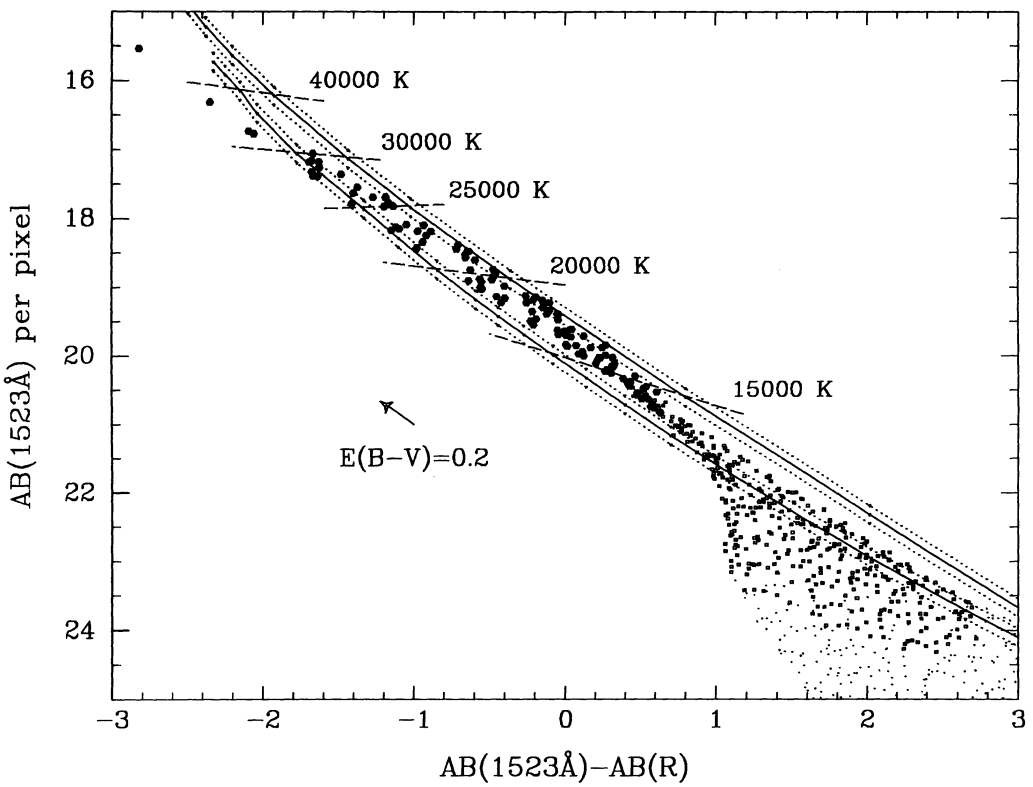

FIG. 10.—Color-magnitude diagram for the accretion disk in UX UMa. Surface brightnesses at 1523 Å are plotted against an ultraviolet-to-optical color index. Different symbols relates to different regions in disk radius: $R < 0.3R_{L1}$ (*filled circles*); $0.3R_{L1} < R < 0.6R_{L1}$ (*open squares*); and $R > 0.6R_{L1}$ (*small dots*). The brighter pixels at inner disk are progressively bluer than the fainter ones at larger radii. The solid lines show blackbody and model atmosphere relationships. The angular scale parameter θ^2 is obtained from the vertical shift required to match the theoretical curves with the observed points. Dotted lines show the 1 σ regions of the fit. Lines of constant temperatures are plotted. A dereddening vector corresponding to $E(B - V) = 0.2$ is shown for reference.

pixels in the outer disk regions, which are more affected by noise and thus have less reliable colors. The solid lines show predicted relations for blackbodies and main-sequence model atmospheres obtained from synthetic photometry over the appropriate bandpasses. The main-sequence line was derived from the spectral models of Buser & Kurucz (1992) with solar composition and surface gravity, and temperatures ranging from 5000 K to 50,000 K. These predicted relations may be shifted vertically in the diagram depending on the assumed angular size of the pixels. The brighter pixels at inner disk are progressively bluer than the fainter ones at larger radii. The slope of the observed correlation is in quite good agreement with that of the theoretical relationships.

The angular scale of the disk is determined by the vertical displacement required to align the theoretical curves with the observed points. The vertical shift in magnitudes per pixel is $5 \log_{10}\theta$, where the angular scale parameter is given by $\theta^2 = (R_{L1}/D)^2 \cos i$, and D is the distance to the system. For R_{L1} and i we use the values derived in § 3.2. If we assume that the emission is blackbody, the best-fit solution gives $\theta_{BB} = 0.99\ R_\odot$ kpc^{-1} and $D_{BB} = 401$ pc. If the emission is best represented by main-sequence stellar spectra then $\theta_{MS} = 1.28\ R_\odot$ kpc^{-1} and $D_{MS} = 312$ pc. A color-color diagram for the accretion disk of UX UMa in the optical range reveals that the inner disk has opaque emission, with colors in between the blackbody and main-sequence lines (Horne 1983). The same behavior was observed for the similar nova-like systems RW Tri (Horne & Stiening 1985) and UU Aqr (Baptista, Steiner, & Horne 1995). Assuming that the spectrum lies in between the main-sequence and blackbody lines and fitting the distribution to be constrained between these two lines we obtain $\theta_{BB+MS} = 1.14 \pm 0.09\ R_\odot$ kpc^{-1} and $D_{BB+MS} = 345 \pm 34$ pc.

The interstellar extinction and reddening of UX UMa have little effect in the determination of θ, and hence on the derived distance, because the dereddening vector in the color-magnitude diagram is nearly parallel to the blackbody and main-sequence lines. UX UMa falls in the border of a $E(B-V) = 0.2$ line in the galactic interstellar extinction contour maps of Lucke (1978). However, Verbunt (1987) and Rutten et al. (1992) analyzed *IUE* spectra and found no evidence of interstellar absorption in UX UMa. We adopt $E(B-V) = 0.0$. A dereddening vector corresponding to $E(B-V) = 0.2$ is shown in Figure 10 for reference. The extinction coefficient A_λ(1523 Å) was obtained by interpolation in the table of Savage & Mathis (1979). Although having no influence on the distance estimate, this correction would affect the intensities in the maps and would result in higher temperatures in the disk.

Table 4 compares our distance estimate with values taken from the literature. The derived distance is consistent with most previous determinations for UX UMa. We note that, despite their own larger estimates, Rutten et al. (1992, 1994) assumed a distance of 250 pc to UX UMa. If our estimate is correct, the intensities in their eclipse maps and spatially resolved spectra may be underestimated by as much as ~ 1.9.

The derived distance scales linearly with R_{L1}, which depends on the mass ratio and the orbital separation according to the approximate relation (Plavec & Kratochvil 1964),

$$R_{L1} = a(0.5 - 0.227 \log q)\ . \qquad (10)$$

Our distance estimate was obtained using the parameters derived in § 3.2. If we adopt the parameters of Smak (1994), $q = 0.68$, $i = 73°$, and $a = 1.51\ R_\odot$, the inferred distance increases to $D = 386$ pc. The uncertainty in the orbital separation is the major contributor to the uncertainty in D.

TABLE 4

DISTANCE ESTIMATES

D (pc)	Reference
>216.....	Bailey 1981
340	Patterson 1984
300	Warner 1987
330	Rutten et al. 1992[a]
290	Rutten et al. 1992[b]
328	Smak 1994
345	This paper

[a] Blackbody fit to spectrum of inner disk.

[b] Fractional contribution of secondary star.

3.4.5. *Radial Temperature Profiles and Mass Accretion Rate*

One of the most basic predictions of the accretion disk theory is that the effective temperature, T_{eff}, of a steady state disk depends on the distance from disk center R as

$$T_{eff}^4 = \frac{3GM_1\dot{M}}{8\pi\sigma R^3}\left[1 - \left(\frac{R_1}{R}\right)^{1/2}\right], \qquad (11)$$

where $\dot{M}$ is the mass transfer rate, R_1 is the inner radius of the disk (which might occur either at the white dwarf surface or at its magnetosphere), and the remaining symbols have their usual meaning. This relation is derived from the fact that, in a steady state, the viscous heating of the disk is balanced at each radius by the radiative cooling from its surface (Shakura & Sunyaev 1973; Pringle 1981). For large radial distances, $R \gg R_1$, the radial dependence reduces to $T_{eff} \propto R^{-3/4}$.

To facilitate comparison with theoretical disk models the intensities in the maps were converted to blackbody brightness temperatures. Radial temperature profiles are plotted in a logarithmic scale in Figure 11. Each temperature shown is the blackbody brightness temperature that reproduces the observed surface brightness at the corresponding pixel for $\theta = 1.14\ R_\odot$ kpc^{-1}—which is equivalent to assuming a distance of 345 pc to UX UMa. The lower curves are in the true temperature scale. The other diagrams were progressively shifted upward by 0.3 dex. For each curve a pair of steady state optically thick disk models is plotted for comparison. The temperature profiles of the wavelength ranges affected by the wind emission are shown in light gray. Simulation tests show that the small leveling off of the observed continuum profiles (both UV and optical) near the disk center ($R \lesssim 0.1\ R_{L1}$) is due to the finite resolution of the maps and to the finite signal-to-noise ratio of the input light curves (see Bruch, Beele, & Baptista 1995).

The radial temperature profiles derived from the UV continuum maps range from 8000 K in the outer disk regions ($R \sim 0.7\ R_{L1}$) to 30,000 K in the inner disk ($R \sim 0.1\ R_{L1}$) and reasonably follow the $T \propto R^{-3/4}$ law for steady mass accretion at a rate of $\dot{M} = 10^{-8.0 \pm 0.2}\ M_\odot\ \mathrm{yr}^{-1}$. This is slightly larger than the value of $\dot{M} = 10^{-8.1}\ M_\odot\ \mathrm{yr}^{-1}$ derived by Rutten et al. (1992) from optical data, probably due to the difference in the assumed distance. The UV continuum profiles are a little flatter than the steady state disk model and the outer parts of the disk are brighter. This explains the discrepancy observed by Mason et al. (1994) when trying to fit the continuum eclipse

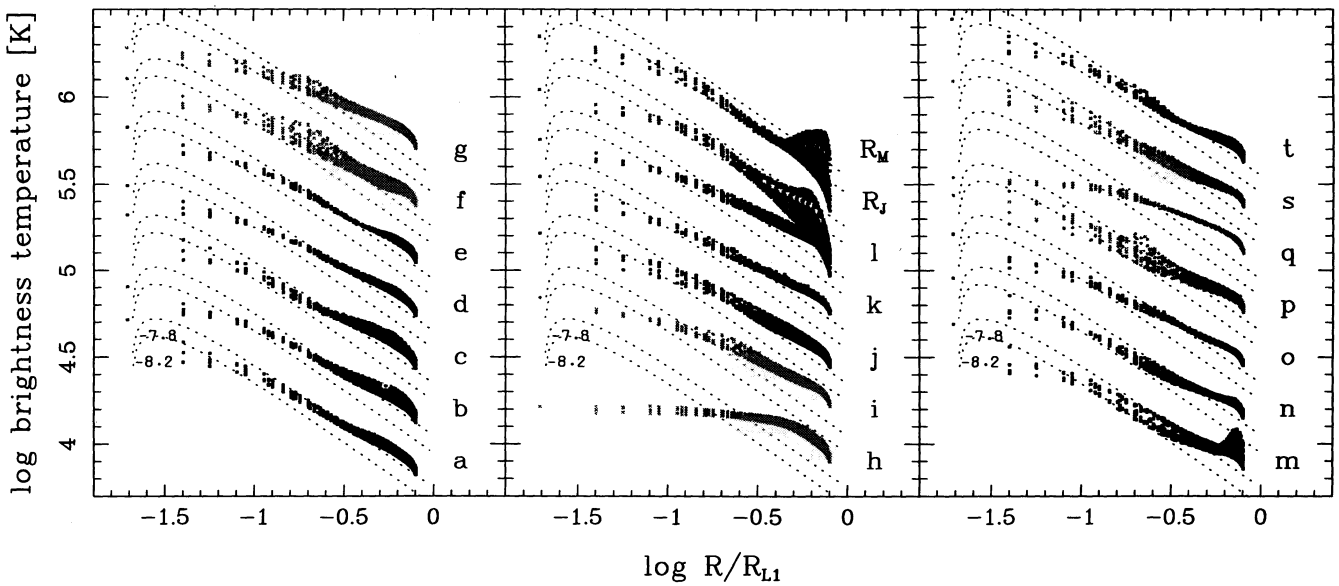

FIG. 11.—Brightness temperature radial profiles. The diagrams were calculated assuming a distance of 345 pc to the system and no reddening. Dotted lines correspond to steady state optically thick disk models for mass accretion rates of $10^{-7.8}$ and $10^{-8.2}$ $M_\odot$ yr^{-1}. The lowest curves are in the true temperature scale. The other diagrams were vertically displaced by 0.3 dex. Abscissas are in units of the distance from the disk center to the inner Lagrangian point (R_{L1}).

shape by assuming a standard disk model emission—which produces a deeper shape at mid-eclipse than observed.

The radial profiles of the Si II line maps (*b* and *d*) seem a bit flatter in the inner regions but otherwise show no perceptible difference with respect to those of the UV continuum. On the other hand, the profiles of the C IV and He II line center maps, *h* and *q*, have a much flatter slope than those of the UV continuum. This could be explained if at these wavelengths the eclipsed part of the line emission arises from an opaque region with a rather uniform spatial intensity distribution as projected in the plane of the sky. The brightness temperatures (and intensities) of these maps remain below those of the adjacent continuum—i.e., the lines appear as absorption features (see § 3.4.7)—up to $R \simeq 0.2\ R_{L1}$.

The radial profile of the *R*-band map of January has a similar slope to those of the UV continuum maps and leads to the same inferred mass accretion rate. This underscores the conclusion that the accretion disk in UX UMa consists of opaque thermal radiators. The bright spot is indicated by the vertical spread of the distribution near $R/R_{L1} \simeq 0.6$. A similar effect is noted in map *m*. However, in this case the structure appears in the opposite side of the bright spot and may be an artifact due to flickering in the corresponding light curve. Note that light curve *m* was obtained from only one data set, run 8. Since no averaging was possible in this case, it is expected that the light curve remains plagued by some flickering.

3.4.6. *Long-Term Changes in the Disk Structure*

In this section we compare the results of the eclipse mapping of the *R*-band data of January and March in an attempt to understand the changes in the orbital light curve observed in Figure 2.

The two light curves with their eclipse mapping fits are seen in Figure 9. The uneclipsed components, marked as dashed lines in both cases, are identical within the uncertainties. This indicates that the observed increase in brightness from January to March must be related to structural changes in the (eclipsed) accretion disk. The *R*-band uneclipsed light is probably due to the contribution of the secondary star to the light at this wavelength range (see Rutten et al. 1992, 1994).

As shown in Figure 9, the disk maps have very similar brightness distributions in their inner regions, with the main differences occurring at large radial distances. The comparison of these maps indicates that the observed brightness change is due to an increase in the disk radius accompanied by a brightening of the bright spot. The increase in the intensity of the bright spot suggests an enhancement in the mass transfer rate from the secondary star. This behavior is consistent with the prediction that the accretion disk increases its radius in response to an increase in the mass transfer rate (Livio & Verbunt 1988).

The radial temperature profiles are plotted in Figure 11. The brightness temperature of the bright spot changes slightly, from $T_{bs} \simeq 9400$ K in January to $T_{bs} \simeq 10{,}200$ K in March.[7] There is no evidence of a significant change in the mass transfer rate, both profiles being in good agreement with a steady state disk model for $\dot{M} = 10^{-8}\ M_\odot$ yr^{-1}. Nevertheless, our ability to measure differences in $\dot{M}$ is limited by the width of the radial profile distribution. Changes of $\lesssim 20\%$ in $\dot{M}$ would remain undetected because they imply a vertical displacement of the radial temperature profile smaller than the width of the observed distribution. Fluctuations in $\dot{M}$ of this magnitude would be enough to explain the observed behavior and to account for the observed change in the brightness temperature of the bright spot.

Mason et al. (1995) have shown that, at the time of the *HST* observations, the UV resonance lines (N V, Si IV, and C IV) were fainter than usual. The decrease in the flux of the UV lines was even more pronounced than that of the adjacent continuum (a similar behavior was also reported by Holm et al. 1982). We have seen that the brightness differences in the *R*-band from the January to the March observations are related to changes

[7] These are in fact lower limits to the true temperatures of the bright spot because its flux is reduced by the azimuthal smearing effect in the eclipse maps.

in the bright spot, probably due to changes in the mass transfer rate. If the March observations are representative of the typical brightness state of UX UMa, the fading in the UV line fluxes could be associated with the fainter bright spot as seen in the *R*-band. Assuming that these UV lines are produced in a disk wind, this correlation may suggest that the amount of matter ejected in the wind (and thus the strength of the emitted lines) is quite sensitive to small fluctuations in the mass transfer rate. It may also suggest that the bright spot itself gives a non-negligible contribution to the emission in the UV resonance lines. A prediction from this latter scenario is that, in its normal brightness state, the eclipse light curves of the UV resonance lines in UX UMa should present an asymmetry in the egress corresponding to the eclipse of the bright spot.

3.4.7. *Spatially Resolved Spectra*

Each of the UV eclipse maps yields spatially resolved information about the emitting region on a specific wavelength range. By combining all 18 narrowband intensity maps we are able to isolate the spectrum of the eclipsed region at any desired position (e.g., Rutten et al. 1993). We divided the maps into five concentric annular regions centered on the white dwarf, labeled in units of R_{L1} in Figure 12. The radial width of the regions is chosen based on the spatial resolution and the signal-to-noise ratio of the intensity maps.

Each spectrum is obtained by averaging the intensity of all pixels inside the corresponding annulus. The statistical uncertainties affecting the average intensities were estimated with a Monte Carlo procedure (e.g., Rutten et al. 1992). For a given narrowband light curve a set of 10 artificial light curves is generated, in which the data points are independently and randomly varied according to a Gaussian distribution with standard deviation equal to the uncertainty at that point. These light curves are fitted with the eclipse mapping algorithm to produce a set of randomized intensity maps. Average intensity values for each of the annular regions are then computed for all the randomized maps. The standard deviation of the average intensities of the randomized maps is taken as the corresponding uncertainty for each annulus. The procedure is repeated for all the narrowband light curves.

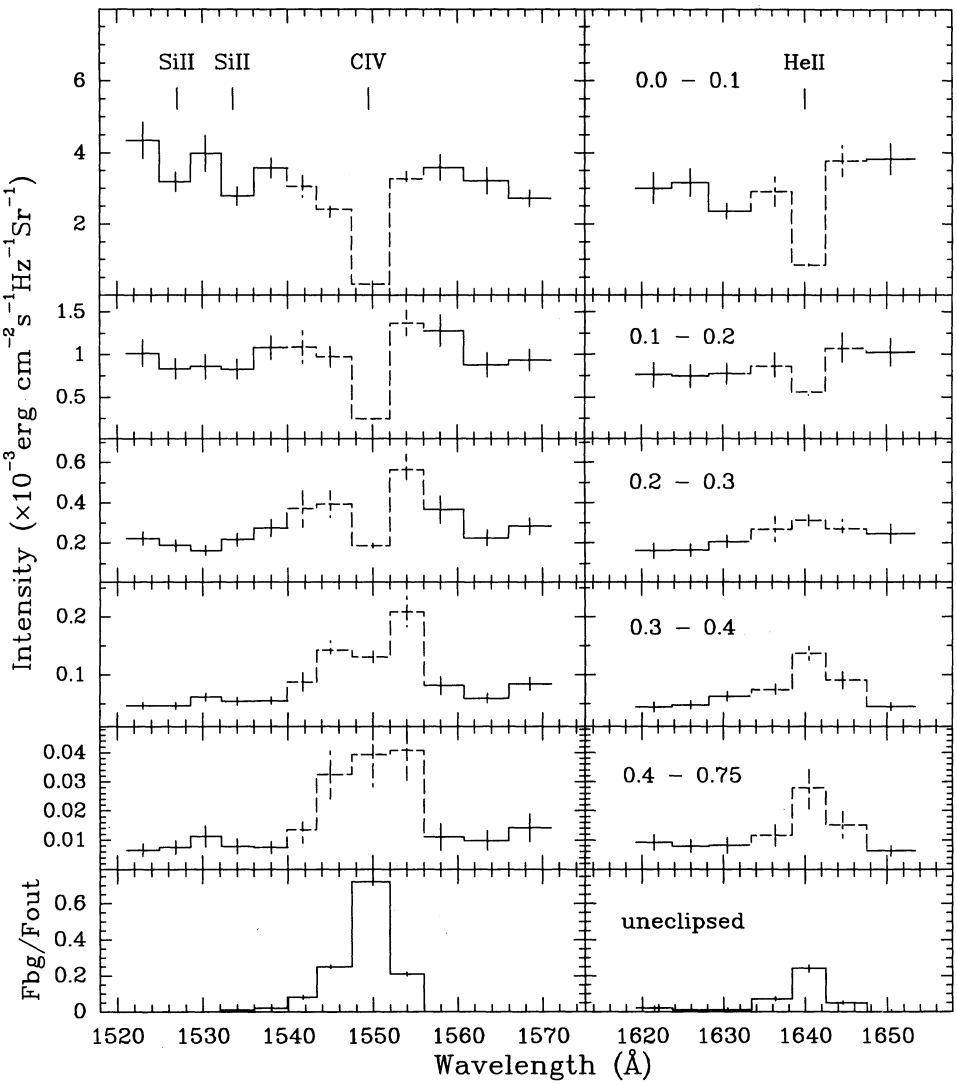

FIG. 12.—Spatially resolved spectra of the accretion disk for the C IV and He II regions. The spectra were obtained by averaging the intensity in all maps for a set of concentric annuli (labeled values in units of R_{L1}). The uneclipsed flux is shown as the ratio with respect to the average out-of-clipse flux at each spectral bin.

The spectrum of each of the annular regions and that of the uneclipsed component are shown in Figure 12. The spectral regions affected by the wind emission are plotted as dashed lines. The uneclipsed flux is shown as the ratio with respect to the average out-of-eclipse flux at each spectral bin.

The sequence of spectra shows that the Si II lines are seen in absorption at the inner disk but disappear into the continuum emission with increasing radius. Both lines show no evidence of uneclipsed light. These lines are possibly formed in the atmosphere of the inner accretion disk instead of the disk wind. The C IV and He II lines show a substantially different behavior. When projected against the bright continuum emission of the inner disk they appear as deep narrow absorption features—which underscores the conclusion that the low-velocity emission in both lines is optically thick (§ 2.4)—but progressively change to broad emission with increasing disk radius because the adjacent continuum distribution falls off much more rapidly with radius (Fig. 11).

The uneclipsed light has an emission-line spectrum with broad C IV and He II components, consistent with the mid-eclipse spectrum shown in Figure 1. At the C IV line center the uneclipsed light accounts for $\simeq 70\%$ of the total light. This confirms the suggestion that this line is dominated by emission from regions outside the orbital plane, probably in a vertically extended accretion disk wind. This is also rather unfortunate, as it tells us that one cannot use the occultation by the secondary star to gain insight into the geometry of the significant fraction of this extended region which completely escapes eclipse. For the He II line center the contribution of the uneclipsed light to the total emitted light is only $\simeq 25\%$, suggesting either a smaller wind component or that the wind emission is much more concentrated toward the orbital plane. There is no sign of a continuum component, e.g., due to the secondary star, in the uneclipsed light. This is not surprising because the spectrum of the cool late-type star is expected to drop sharply in the UV and should yield a negligible contribution to the total light at these wavelengths.

The facts that a substantial fraction of the light in both the C IV and He II lines completely escapes eclipse and that the mapped portion of the emission in these lines still shows significant emission in the outer regions where the adjacent continuum has already faded indicate that the line emitting region is much larger than the continuum region, in accordance with the inferences drawn in § 2.4.

It is worth mentioning that this same pattern of absorption in the inner disk changing to emission in the outer disk associated with significant uneclipsed light is also found by Rutten et al. (1994) for the Balmer lines, suggesting the possibility that they too have a wind component.

4. DISCUSSION

4.1. *Reliability of the Binary Parameters*

The technique envisaged by Wood et al. (1985) to extract the contact phases of the white dwarf from the eclipse light curves yield proper and reliable results for relatively high signal-to-noise data. The fairly large amount of smoothing needed to apply the technique to the UX UMa continuum light curves may distort the derivative curve by reducing sharp features and redistributing the flux in the phase axis. This could result in systematically larger $\Delta\phi_{wd}$ values and lower integrated fluxes f_{wd}. In this case, the photometric relation in the primary-secondary mass diagram would be a lower limit boundary for the mass of the white dwarf, and both derived white dwarf mass and temperature would be lower limits to the true values. If the white dwarf flux is underestimated the eclipse light curve after subtracting the white dwarf component (Fig. 6*e*) would present a perceptible change in slope during ingress/egress due to the residual white dwarf contribution. The fact that there is no significant break in the slope of the disk light curve across ingress and egress gives confidence that the estimated $\Delta\phi_{wd}$ and f_{wd} values are not significantly affected by this effect.

The binary parameters in § 3.2 were derived under the assumption that the radius of the white dwarf is given by the duration of the ingress/egress of the central object, $\Delta\phi_{wd}$. This supposition may not always be correct. It may be possible that the observed compact object of Figure 7 is a hot and opaque boundary layer involving the white dwarf, in which case the true white dwarf would be smaller than assumed (Wood & Crawford 1986). In this case, the primary mass found is a lower limit. Increasing the white dwarf mass would bring the secondary star closer to the main sequence. Other effects that may result in an overestimated white dwarf radius include the inappropriate application of a mass-radius relation for cool white dwarfs to a quite hot object (Horne, Wood, & Stiening 1991), and a possible spherical distortion for a white dwarf rotating close to breakup velocity (Wood & Horne 1990). However, we do not take these effects into consideration because the implied corrections ($\sim 5\%$) are small compared to the uncertainties affecting the calculated parameters.

Our parameters are consistent with the ranges given by Smak (1994), although his nominal value for the white dwarf mass, $M_1 = 0.7\ M_\odot$, is larger than our estimate and the implied mass ratio is therefore smaller ($q = 0.68$). This primary mass would imply a $\Delta\phi_{wd} \simeq 0.005$ cycles, significantly smaller than the measured value. We note that in his model Smak assumed a secondary on the main sequence and neglected the isotropic component of the bright spot emission, which may lead to systematic errors in the derived parameters.

A major source of uncertainty affecting the binary parameters is the mass ratio, q. A more reliable determination of q can be obtained from the eclipse phases of the bright spot (e.g., Wood et al. 1986, 1989). Unfortunately the bright spot seems too faint and too red to be seen at the UV wavelengths of this study. If the bright spot has $T \simeq 10^4$ K, the best region to look for it in the light curves is in the range $\simeq 2000$–3000 Å, where its emission would peak and where it should be relatively brighter compared with the disk emission.

4.2. *Incompatibility between* $\dot{P}$ *and* $\dot{M}$*?*

An upper limit to the mass transfer rate in UX UMa can be obtained from the derived upper limit on the rate of secular change in its orbital period (§ 3.1) as follows. We start by adopting a mass-radius relation of the form $R_2(t) \propto M_2(t)^\beta$, and we assume that the radius of the secondary star is given by the equivalent radius of its Roche lobe,

$$\frac{R_2}{a} = 0.462\left(\frac{M_2}{M_1 + M_2}\right)^{1/3} . \tag{12}$$

Equation (12) is accurate to better than 4% for mass ratios $q \simeq 1$. Using Kepler's third law to eliminate the orbital separation we obtain (e.g., Robinson, Shetrone, & Africano 1991),

$$M_2^{(3\beta-1)} \propto P^2 . \tag{13}$$

Differentiating the above expression with respect to time one

finds a relation between $\dot{P}$ and $\dot{M}_2$,

$$\frac{\dot{M}_2}{M_2} = \frac{2}{3\beta - 1}\frac{\dot{P}}{P}, \quad (14)$$

which is independent of any assumption about mass and angular momentum loss in the binary. Using the upper limit in equation (2) and assuming the mass-radius relation of Caillault & Patterson (1990) for the lower main-sequence, $\beta \simeq 0.8$, we obtain $\dot{M}_2 < 1.6 \times 10^{-9}\ M_\odot\ \mathrm{yr}^{-1}$. This upper limit is almost an order of magnitude *smaller* than the mass transfer rate derived from the radial temperature profiles in § 3.4.5.

One could try to reconcile the derived values of $\dot{M}$ by varying the value of β. However, the inferred mass transfer rates only become compatible for unreasonably low values, $\beta \lesssim 0.4$. Another alternative is to consider that the $\dot{M}$ derived from the eclipse mapping corresponds to an instantaneous value while the above $\dot{M}$ is an average over a much longer time base. However, this would imply that, on average during the last $\sim$40 yr, UX UMa would have been some 2.5 mag fainter than during our observations!

One possible way to understand the inconsistency is by looking at the $(O - C)$ diagram of Figure 5. UX UMa shows conspicuous cyclical period changes that cannot be explained in terms of a third body or apsidal motion, but may be related to a magnetic activity cycle in the secondary star (see Marsh & Pringle 1990 and Applegate 1992 for recent reviews on the topic). These period changes are much larger than those possibly produced by the secular evolution. In this regard, the above upper limit on $\dot{M}$ could be understood as the maximum mass transfer rate UX UMa would have (due to secular evolution) in the absence of its cyclical period variations. Since the value of $\dot{M}$ inferred in § 3.4.5 is much larger than the above limit, we may conclude that the secular evolution is not responsible for the high-mass transfer rate observed in UX UMa. Instead, the high inferred $\dot{M}$ value may be connected to the same physical mechanism responsible for the observed cyclical period changes.

At the present time there is no clear detection of secular period changes in CVs. For the systems that have a long enough observational time base to prevent the confusion between the secular trend and the cyclical variations there are at most upper limits on $\dot{P}$ (Robinson et al. 1991; Rubenstein et al. 1991; Smak 1993). It will be interesting to check whether the above conclusion will hold for the other high mass transfer systems as longer observational time bases enable more stringent limits on $\dot{P}$ to be inferred.

5. SUMMARY

We present the results of a study of the nova-like system UX UMa based on *HST* time-resolved spectroscopy in the ultraviolet and on simultaneous *R*-band optical photometry. The major findings of our study are

1. The eclipses in the UV continuum are deep, nearly reaching the zero level at mid-eclipse phases. Sharp ingress and egress features reveal the occultation of the white dwarf at the disk center but there is no evidence of the orbital hump or of the bright spot.

2. Velocity-resolved light curves in the C IV λ1550 line show asymmetric eclipse shapes indicating a rotational disturbance in this line. A conspicuous orbital modulation is seen in the line center light curve and a smaller effect is also noted in the light curve of the red wing, suggesting either velocity-dependent anisotropic emission, the anisotropy being stronger at lower velocities and for redshifted emission, or that significant absorption occurs at orbital phase $\sim$0.5, where the secondary star and the bright spot region are behind the disk and its extended atmosphere.

3. By combining our new measured eclipse timings with those previously published we obtain a revised linear ephemeris for the eclipses in UX UMa. We find an upper limit for orbital period variations of $|\dot{P}| < 1.3 \times 10^{-12}\ \mathrm{s\ s}^{-1}$.

4. We used the steep ultraviolet eclipse light curves to measure contact phases of the white dwarf. The radius of the white dwarf is obtained from the duration of its ingress/egress feature in the eclipse light curve. This yields a steep relation in the primary-secondary mass diagram which constrains the white dwarf mass to a narrow region. By combining this relation with the primary mass function of Shafter (1984) and with the assumption that the secondary is a main-sequence star we obtain $M_1 = M_2 = 0.47\ M_\odot$. The adopted binary parameters are collected in Table 3.

5. The white dwarf contributes with $\simeq$25% of the light at 1600 Å. If the inner disk is optically thick it has a temperature of $T_{\mathrm{wd}} \gtrsim 65{,}000$ K. The predicted flux at 5500 Å is 0.7 mJy, or $\sim$3% of the out-of-eclipse flux at this wavelength.

6. No oscillations were detected in the *HST* data. We found an upper limit of 0.02 mags for oscillations in the range 0.002–0.1 Hz.

7. Maximum-entropy eclipse mapping techniques were used to solve for maps of the disk brightness distribution and for fluxes of an additional uneclipsed component in 18 narrow UV bands near the C IV λ1550 and He II λ1640 regions and in the *R*-band. The maps in the C IV and He II line profiles are affected by emission from the disk wind. The radial brightness temperature profiles of both line center maps show a flat slope. It is suggested that at these wavelengths the eclipsed part of the line emission arises from an opaque extended region with a rather uniform spatial intensity distribution as projected in the plane of the sky. When plotted as a sequence of spatially resolved spectra these lines appear as deep narrow absorption features at disk center and change to broad emission in the outer disk regions besides showing large uneclipsed components. This behavior is similar to the one found by Rutten et al. (1994) for the Balmer lines and suggests that these optical lines may also have a wind component.

8. The angular scale of the disk and the distance to UX UMa are estimated from a color-magnitude diagram by a method similar to cluster main-sequence fitting. If the inner disk has emission in between the blackbody and main-sequence lines, the angular scale parameter $\theta = (R_{\mathrm{L1}}/D)\sqrt{\cos i}$ is found to be $\theta = 1.14 \pm 0.09\ R_\odot\ \mathrm{kpc}^{-1}$. The corresponding distance is $D = 345 \pm 34$ pc.

9. The radial temperature profiles derived from the UV continuum maps range from 8000 K in the outer disk regions to 30,000 K in the inner disk and reasonably follow the $T \propto R^{-3/4}$ law for steady mass accretion at a rate of $\dot{M} = 10^{-8.0 \pm 0.2}\ M_\odot\ \mathrm{yr}^{-1}$.

10. The spatially resolved spectra suggest that the Si II $\lambda\lambda$1527, 1533 absorption lines are formed in the atmosphere of the inner disk.

11. The comparison of the *R*-band eclipse maps indicates that the observed increase in brightness from January to March is due to an increase in the disk radius accompanied by a brightening of the bright spot, probably due to a small

TABLE 5

SPATIALLY RESOLVED SPECTRA OF UX URSAE MAJORIS

		Regions[a]											
		0.0–0.1 R_{L1}		0.1–0.2 R_{L1}		0.2–0.3 R_{L1}		0.3–0.4 R_{L1}		0.4–0.75 R_{L1}		Uneclipsed	
Map	λ (Å)	I_ν	σ	I_ν	σ	I_ν	σ	I_ν	σ	I_ν	σ	F_{bg}	σ
a	1523.0	4.34E − 3	(0.5)	1.01E − 3	(0.15)	2.22E − 4	(0.3)	4.64E − 5	(0.6)	6.55E − 6	(2.0)	3.88E − 2	(1.4)
b	1526.8	3.18E − 3	(0.3)	8.31E − 4	(1.2)	1.88E − 4	(0.3)	4.64E − 5	(0.6)	7.52E − 6	(2.3)	4.75E − 2	(2.3)
c.....	1530.3	3.98E − 3	(0.5)	8.56E − 4	(1.4)	1.64E − 4	(0.2)	6.15E − 5	(0.7)	1.13E − 5	(0.4)	5.54E − 2	(1.5)
d	1534.0	2.78E − 3	(0.3)	8.27E − 4	(1.1)	2.17E − 4	(0.3)	5.37E − 5	(0.7)	7.89E − 6	(2.5)	1.72E − 1	(0.7)
e.....	1538.0	3.57E − 3	(0.3)	1.08E − 3	(0.14)	2.74E − 4	(0.4)	5.49E − 5	(0.6)	7.47E − 6	(2.0)	3.29E − 1	(0.8)
f.....	1541.7	3.05E − 3	(0.3)	1.08E − 3	(0.19)	3.71E − 4	(0.9)	8.73E − 5	(1.6)	1.35E − 5	(0.4)	1.77	(0.23)
g	1545.0	2.41E − 3	(0.2)	9.73E − 4	(1.2)	3.91E − 4	(0.6)	1.42E − 4	(0.16)	3.24E − 5	(0.8)	6.64	(0.37)
h	1550.0	3.09E − 4	(0.2)	2.45E − 4	(0.2)	1.87E − 4	(0.1)	1.31E − 4	(0.09)	3.93E − 5	(1.1)	25.00	(0.54)
i.....	1554.0	3.27E − 3	(0.2)	1.37E − 3	(0.15)	5.63E − 4	(0.7)	2.08E − 4	(0.26)	4.08E − 5	(1.1)	7.16	(0.33)
j.....	1558.0	3.59E − 3	(0.4)	1.28E − 3	(0.19)	3.65E − 4	(0.7)	8.10E − 5	(1.5)	1.11E − 5	(0.5)	3.44E − 2	(1.4)
k	1563.5	3.21E − 3	(0.4)	8.75E − 4	(1.4)	2.25E − 4	(0.4)	5.92E − 5	(0.8)	9.89E − 6	(3.4)	4.96E − 2	(1.7)
l.....	1568.5	2.72E − 3	(0.2)	9.32E − 4	(1.3)	2.83E − 4	(0.4)	8.36E − 5	(1.0)	1.42E − 5	(0.5)	1.02E − 1	(0.3)
m.....	1621.5	3.00E − 3	(0.4)	7.60E − 4	(1.4)	1.62E − 4	(0.4)	4.41E − 5	(0.8)	9.14E − 6	(2.6)	3.69E − 1	(1.2)
n	1626.0	3.16E − 3	(0.4)	7.44E − 4	(1.3)	1.64E − 4	(0.3)	4.76E − 5	(0.7)	7.92E − 6	(2.2)	1.78E − 1	(0.4)
o	1630.5	2.36E − 3	(0.2)	7.72E − 4	(1.2)	2.06E − 4	(0.3)	6.20E − 5	(0.8)	8.16E − 6	(2.6)	1.71E − 1	(0.6)
p	1636.4	2.91E − 3	(0.4)	8.59E − 4	(1.6)	2.67E − 4	(0.6)	7.37E − 5	(1.3)	1.17E − 5	(0.4)	1.30	(0.23)
q	1640.5	8.40E − 4	(0.2)	5.59E − 4	(0.4)	3.12E − 4	(0.3)	1.36E − 4	(0.11)	2.79E − 5	(0.7)	4.25	(0.31)
s.....	1644.6	3.77E − 3	(0.4)	1.06E − 3	(0.20)	2.70E − 4	(0.5)	9.01E − 5	(1.4)	1.51E − 5	(0.5)	1.00	(0.21)
t.....	1650.5	3.82E − 3	(0.4)	1.02E − 3	(0.16)	2.45E − 4	(0.5)	4.48E − 5	(0.7)	6.31E − 6	(1.7)	4.21E − 2	(1.2)
R	6585.0	9.56E − 4	(0.3)	6.03E − 4	(0.4)	3.33E − 4	(0.3)	1.66E − 4	(0.14)	5.93E − 5	(1.5)	5.14	(0.45)

[a] Specific intensities I_ν in ergs cm^{-2} s^{-1} Hz^{-1} Sr^{-1}, uneclipsed component F_{bg} in mJy. The numbers in parentheses are the uncertainties in the preceding column, under the exponent.

($\lesssim$20%) enhancement in the mass transfer rate from the secondary star.

12. The upper limit on $\dot{M}$ obtained from the derived upper limit on the secular period change is almost an order of magnitude smaller than the mass transfer rate inferred from the radial temperature profiles, which suggests that the high mass transfer rate of UX UMa is not the consequence of its secular period decrease.

We thank René Rutten for stimulating discussions on eclipse mapping techniques, Mario Livio for useful comments on evolutionary aspects of CVs, and Christian Knigge and Alon Retter for interesting discussions about disk wind models and geometries. We are grateful to the referee for valuable comments on the original manuscript. K. O. M. acknowledges the support of the Royal Society of London. J. E. D. acknowledges the support of an Advanced Fellowship funded by the Particle Physics and Astronomy Research Council of the United Kingdom. This work was supported by NASA grant GO-3578 from the STScI (which is operated by AURA under NASA contract NAS 5-26555) and by the Long Term Space Astrophysics Research Program grant NAGW-2678.

REFERENCES

Africano, J., & Wilson, J. 1976, PASP, 88, 8
Applegate, J. H. 1992, ApJ, 385, 621
Bailey, J. 1979, MNRAS, 187, 645
———. 1981, MNRAS, 197, 31
Baptista, R., Jablonski, F. J., & Steiner, J. E. 1989, MNRAS, 241, 631
Baptista, R., & Steiner, J. E. 1991, A&A, 249, 284
———. 1993, A&A, 277, 331
Baptista, R., Steiner, J. E., & Horne, K. 1995, in preparation
Bell, S. A., Hilditch, R. W., & Edwin, R. P. 1993, MNRAS, 260, 478
Bessell, M. 1983, PASP, 95, 480
Bruch, A., Beele, D., & Baptista, R. 1995, A&A, submitted
Buser, R., & Kurucz, R. L. 1992, A&A, 264, 557
Caillault, J. P., & Patterson, J. 1990, AJ, 100, 825
Cordova, F. A., & Mason, K. O. 1985, ApJ, 290, 671
Drew, J. E. 1987, MNRAS, 224, 595
Hamada, T., & Salpeter, E. E. 1961, ApJ, 134, 683
Holm, A. V., Panek, R. J., & Schiffer, F. H. 1982, ApJ, 252, L35
Horne, K. 1983, Ph.D. thesis, Caltech
———. 1985, MNRAS, 213, 129
———. 1993, in Accretion Disks in Compact Stellar Systems, ed. J. C. Wheeler (Singapore: World Scientific), 117
Horne, K., & Stiening, R. F. 1985, MNRAS, 216, 933
Horne, K., Wood, J. H., & Stiening, R. F. 1991, ApJ, 378, 271
King, A. R., Frank, J., Jameson, R. F., & Sherrington, M. R. 1983, MNRAS, 203, 677
Knigge, C., et al. 1995, in preparation
Knigge, C., Drew, J. E., Hoare, M. G., & la Dous, C. 1994, MNRAS, 269, 891
Kukarkin, B. V. 1977, MNRAS, 180, 5P
Lamla, E. 1981, Landolt-Börnstein–Numerical Data and Functional Relationships in Science and Technology, Vol. 2, ed. K. Schaifers & H. H. Voigt (Berlin: Springer)
Landolt, A. U. 1983, AJ, 78, 959
Livio, M., & Verbunt, F. 1988, MNRAS, 232, 1P
Lucke, P. B. 1978, A&A, 64, 367
Marsh, T. R., & Pringle, J. E. 1990, ApJ, 365, 677
Mason, K. O., Drew, J. E., Cordova, F. A., Horne, K., Hilditch, R. W., Knigge, C., Lanz, T., & Meylan, T. 1995, MNRAS, submitted
Massey, P., Strobel, K., Barnes, J. V., & Anderson, E. 1988, ApJ, 328, 315
Nather, R. E., & Robinson, E. L. 1974, ApJ, 190, 637
Nauenberg, M. 1972, ApJ, 175, 417
Patterson, J. 1984, ApJS, 54, 443
Plavec, M., & Kratochvil, P. 1964, Bull. Astron. Inst. Czechoslovakia, 15, 165
Press, W. H., Flannery, B. P., Teukolsky, S. A., & Vetterling, W. T. 1986, Numerical Recipes (Cambridge: Cambridge Univ. Press)
Pringle, J. 1975, MNRAS, 170, 633
———. 1981, ARA&A, 19, 137
Quigley, R., & Africano, J. L. 1978, PASP, 90, 445
Ritter, H. 1980, A&A, 86, 204
Robinson, E. L., Shetrone, M. D., & Africano, J. L. 1991, AJ, 102, 1176
Rubenstein, E. P., Patterson, J., & Africano, J. L. 1991, PASP, 103, 1258
Rutten, R. G. M., Dhillon, V. S., Horne, K., & Kuulkers, E. 1994, A&A, 283, 441
Rutten, R. G. M., Dhillon, V. S., Horne, K., Kuulkers, E., & van Paradijs, J. 1993, Nature, 362, 518
Rutten, R. G. M., van Paradijs, J., & Tinbergen, J. 1992, A&A, 260, 213
Savage, B. D., & Mathis, J. S. 1979, ARA&A, 17, 73
Shafter, A. 1984, AJ, 89, 1555
Shakura, N. I., & Sunyaev, R. A. 1973, A&A, 24, 337
Shortridge, K. 1987, Starlink FIGARO Users Guide, Rutherford Appleton Laboratory, UK
Sion, E. M. 1985, ApJ, 297, 538
———. 1987, Ap&SS, 130, 47

Skilling, J. 1987, in Maximum Entropy and Bayesian Methods in Applied Statistics, ed. J. H. Justice (Cambridge: Cambridge Univ. Press), 156
Skilling, J., & Bryan, R. K. 1984, MNRAS, 211, 111
Smak, J. 1993, Acta Astron., 43, 121
———. 1994, Acta Astron., 44, 59
Verbunt, F. 1987, A&AS, 71, 339
Warner, B. 1987, MNRAS, 227, 23
Warner, B., & Nather, R. E. 1972, MNRAS, 159, 429
Wood, J. H., & Crawford, C. S. 1986, MNRAS, 222, 645
Wood, J. H., & Horne, K. 1990, MNRAS, 242, 609
Wood, J. H., Horne, K., Berriman, G., & Wade, R. 1989, ApJ, 341, 974
Wood, J. H., Horne, K., Berriman, G., Wade, R., O'Donoghue, D., & Warner, B. 1986, MNRAS, 219, 629
Wood, J. H., Irwin, M. J., & Pringle, J. E. 1985, MNRAS, 214, 475